Full Length Article

Mineral tessellation in mouse enthesis fibrocartilage, Achilles tendon, and *Hyp* calcifying enthesopathy: A shared 3D mineralization pattern

Daniel J. Buss [a], Katya Rechav [b], Natalie Reznikov [a,c,d], Marc D. McKee [a,d,*]

[a] *Department of Anatomy and Cell Biology, School of Biomedical Sciences, Faculty of Medicine and Health Sciences, McGill University, Montreal, Quebec, Canada*
[b] *Electron Microscopy Unit, Weizmann Institute of Science, Rehovot, Israel*
[c] *Department of Bioengineering, Faculty of Engineering, McGill University, Montreal, Quebec, Canada*
[d] *Faculty of Dental Medicine and Oral Health Sciences, McGill University, Montreal, Quebec, Canada*

ABSTRACT

The hallmark of enthesis architecture is the 3D compositional and structural gradient encompassing four tissue zones – tendon/ligament, uncalcified fibrocartilage, calcified fibrocartilage and bone. This functional gradient accommodates the large stiffness differential between calcified bone and uncalcified tendon/ligament. Here we analyze in 3D the organization of the mouse Achilles enthesis and mineralizing Achilles tendon in comparison to lamellar bone. We use correlative, multiscale high-resolution volume imaging methods including μCT with submicrometer resolution and FIB-SEM tomography (both with deep learning-based image segmentation), and TEM and SEM imaging, to describe ultrastructural features of physiologic, age-related and aberrant mineral patterning. We applied these approaches to murine wildtype (WT) Achilles enthesis tissues to describe in normal calcifying fibrocartilage a crossfibrillar mineral tessellation pattern similar to that observed in lamellar bone, but with greater variance in mineral tesselle morphology and size. We also examined Achilles enthesis structure in *Hyp* mice, a murine model for the inherited osteomalacic disease X-linked hypophosphatemia (XLH) with calcifying enthesopathy. In Achilles enthesis fibrocartilage of *Hyp* mice, we show defective crossfibrillar mineral tessellation similar to that which occurs in *Hyp* lamellar bone. At the cellular level in fibrocartilage, unlike in bone where enlarged osteocyte mineral lacunae are found as peri-osteocytic lesions, mineral lacunar volumes for fibrochondrocytes did not differ between WT and *Hyp* mice. While both WT and *Hyp* aged mice demonstrate Achilles tendon midsubstance ectopic mineralization, a consistently defective mineralization pattern was observed in *Hyp* mice. Strong immunostaining for osteopontin was observed at all mineralization sites examined in both WT and *Hyp* mice. Taken together, this new 3D ultrastructural information describes details of common mineralization trajectories for enthesis, tendon and bone, which in *Hyp*/XLH are defective.

1. Introduction

Vertebrates apply muscle contraction forces to facilitate movement. These forces are transmitted to rigid bone through tendon insertion sites called entheses. Entheses are remarkably adapted to the extreme mechanical challenges that arise when loading must be repeatedly transmitted across tissues with a stiffness differential of two orders of magnitude. While flexible tendons dissipate stress by deformation, mature mineralized cartilage and bone tissue resist deformation, as mineralization renders them stiff [1,2]. At insertion sites of tendon into bone, a specialized tissue complex – enthesis fibrocartilage – provides a gradient in extracellular matrix properties that acts to minimize stress

concentration [3–6].

The unique stiffness gradient found across the enthesis – which remarkably spans as little as only hundreds of micrometers in the mature enthesis of mice – develops as a result of complex gene expression patterns during development [7,8]. In turn, these developmental cues result in defined zones with varying extracellular matrix composition and organization, and with distinct mineralization and hydration status. The mature fibrocartilage enthesis attachment is classically described as having four zones as defined by the resident cell type and by the proteins that they produce [3,5].

The first two zones starting from the tendon/ligament side normally do not undergo mineralization (calcification). In the tendon zone, the

extracellular matrix type I collagen fibrils are closely packed and crosslinked, and with neighboring fibrils form larger, highly aligned (anisotropic) fibril bundles/fibers, which collectively resist tensile forces. Positioned amongst the type I collagen arrays are elongated tenocytes aligned along the long axis of the collagen, with thin cytoplasmic extensions that stretch out into the extracellular matrix [9,10]. The second region – the uncalcified enthesis fibrocartilage (UF) zone – is broadly characterized by the combination of type I collagen matrix with type II collagen and proteoglycan, the latter with its glycosaminoglycan content that binds water, this being a hydration feature that enhances resistance to compression [11]. This zone also features changes in fiber orientation [4]. As opposed to the elongated tenocytes of the tendon zone, uncalcified fibrocartilage is populated by more rounded fibrochondrocyte cells, decorated by abundant and regularly spaced filopodial extensions [10,12].

In the next two zones, extracellular matrix mineralization occurs to provide a rigid, robust anchoring mechanism. In terms of mineralization-regulating molecules, the third region called the calcified fibrocartilage (CF) zone additionally incorporates type X collagen [3] and osteopontin (OPN) into the extracellular matrix [13], along with differential expression of enzymes known to favor mineralization such as tissue-nonspecific alkaline phosphatase (TNAP). TNAP degrades small-molecule inhibitors of mineralization such as pyrophosphate (PPi) to promote mineralization [14–16]. The variation in mineral content and organization in this zone provides a gradient from less-mineralized to more-mineralized extracellular matrix towards the heavily mineralized bone tissue [17–19], potentially further diffusing stress concentration. In addition to these "macroscale" tissue features imparted by mineralization, it has been suggested that at the scale of tens to hundreds of micrometers, discrete mineralization events collectively form a corrugated mineralization front in the fibrocartilage, thus additionally acting as a toughening mechanism by increasing the contact area between compliant and stiff components into a three-dimensional interface [20]. Fibrochondrocytes in the calcified fibrocartilage zone become surrounded by mineral (to form mineral lacunae), either partially or fully depending upon their proximity to the mineralization front. An interdigitated cement line (presumably also as a stress dissipation architectural feature [4,21]) demarcates the transition to the fourth enthesis zone — bone.

There are certain skeletal diseases in which the fine spatial and temporal control of mineralization is disrupted. In the osteomalacic (and odontomalacic) inherited disease X-linked hypophosphatemia (XLH), and in the *Hyp* mouse model of this disease studied here, bones and teeth are hypomineralized [22–25]. Bones deform through bending, buckling, and fracturing, and calcifying enthesopathy is a common occurrence [26–28]. In XLH, inactivating mutations in the *PHEX* gene (that encodes the transmembrane endopeptidase phosphate-regulating endopeptidase homolog X-linked normally expressed by osteocytes, osteoblasts, and odontoblasts) results in elevated levels of systemic circulating FGF23 causing renal phosphate wasting [29]. Locally in the extracellular matrix, *PHEX* mutations result in an accumulation of mineralization-inhibiting osteopontin that likewise contributes to the hypomineralization phenotype [23]. In XLH, paradoxical ectopic calcification often occurs as expansion of the calcified fibrocartilage of the enthesis — called calcifying enthesopathy – at various tendon and ligament insertion sites, and at a relatively early age of adulthood for many patients, leading to further loss of mobility and additional pain [15,26–28,30].

To date, for normal enthesis, beyond structure obtained from conventional radiography, micro-computed tomography and histology studies, much less is known about the nano- to microscale 3D structure of the insertion site in terms of its mineralization events and patterns. In contrast, we have recently described the trajectory of the microscale 3D space-filling mineralization pattern in lamellar bone known as "crossfibrillar mineral tessellation" [24,31,32]. Similarly, beyond just a few studies attempting to address XLH enthesopathy in the commonly used *Hyp* mouse model (having truncating mutations in the *Phex* gene)

[14,15,30,33,34], there exists no information on the ultrastructure of XLH/*Hyp* enthesis. Given the prevalence of 3D microscale mineral tessellation in normal bone across different species [31], we hypothesized that this structural feature may also appear within calcified enthesis fibrocartilage and therefore contribute to the properties of the normal attachment site, and that it might be altered in *Hyp* mice. Here we provide new comparative 3D multiscale information on mineralization in normal (wildtype, WT) and osteomalacic (*Hyp*) Achilles enthesis and Achilles midsubstance tendon (respectively representing physiologic and ectopic mineralization), in mice of different postnatal ages. Several recent original research articles and reviews have detailed the necessity of assessing mineralized tissues in a correlative fashion, with analysis of nanoscale features (and in 3D) through to the microscale, which collectively provide an explanation for the origin of macroscale mechanical properties [35–38]. In addition to new ultrastructural observations in normal and *Hyp* mice, we also discuss the molecular mechanisms which may influence the trajectory of physiologic, ectopic and altered mineralization.

2. Material and methods

2.1. Rationale for a multiscale 3D imaging approach to study enthesis and tendon mineralization

Given the nanoscale structure of mineral crystallites within the collagenous extracellular matrix of bone, together with their microscale crossfibrillar tessellation [24,31] – a packing pattern that contributes to bone's remarkable combination of stiffness and toughness – it has become imperative to assess other mineralized tissues in this same correlative and contextualized 3D manner. Here, we use a variety of multi-scale imaging approaches previously used for normal (wildtype) and osteomalacic (*Hyp*) bone [24] to characterize enthesis.

This mouse study was designed to investigate normal Achilles tendon enthesis structure and mineralization in 3D using multiscale X-ray and electron microscopy tomographic methods, with an additional comparison to enthesis structure found in the osteomalacic X-linked hypophosphatemia (XLH) *Hyp* mouse model. Fortuitously, additional mineralization findings were discovered for Achilles tendon proper (midsubstance) in both WT and *Hyp* mice.

2.2. Animal models and tissue harvesting

Hindlimbs, including the feet and Achilles tendon, were obtained from normal male C57BL/6 wildtype (WT) and mutant *Hyp* mice (B6.Cg-*Phex^Hyp*/J) mice of different ages (The Jackson Laboratory, Bar Harbor, ME, USA). *Hyp* mice have a loss-of-function truncation in the *Phex* gene [39,40] and are a commonly used mouse model for X-linked hypophosphatemia. To date, at the ultrastructural level at which we are looking by electron microscopy for changes between normal WT and *Hyp* mouse mineralized tissues, we have not detected differences in respective mineralization patterns between the sexes. For the *Hyp* mice used here, although both males and females lack a functional *Phex* gene and show osteomalacia, mild gene-dosage effects have been noted between heterozygous and homozygous females [41]. Located on the X chromosome, the *PHEX/Phex* gene is under the control of dosage compensation by random X chromosome inactivation [42] – half the cells in the heterozygous females express normal *PHEX/Phex* allele, and the other half express mutant allele. To avoid confounding gene dosage effects, and to ensure that we can compare findings appropriately to the published literature, only male mice were used in this study. All animal procedures were reviewed and approved by the McGill University Institutional Animal Care and Use Committee, and they followed the guidelines of the Canadian Council on Animal Care. After mouse sacrifice, hindlimbs were dissected and trimmed to isolate the calcaneus with Achilles tendon and plantar fascia attached, and immediately placed in the chemical fixatives mentioned below. In this study, a total of 30 mice

(15 WT and 15 *Hyp*) were examined by various imaging methods, and some tissue samples were examined by multiple methods. The mice ranged in age from 2 to 14 months-old.

2.3. X-ray imaging

2.3.1. Sample preparation and imaging

Hindlimbs from WT and *Hyp* mice at 3.5, 7, 10.5 and 14 months of age were used for μCT X-ray imaging after fixation of the tissues in 4 % paraformaldehyde (Thermo Fisher Scientific, Waltham, MA, USA) and 1 % glutaraldehyde (Electron Microscopy Sciences, Hatfield, PA, USA) in 0.1 M sodium cacodylate buffer (Electron Microscopy Sciences), pH 7.3. Specimens were fixed at room temperature for 2 h on a rotator followed by a 48 h fixation period at 4 °C. After several washes in 0.1 M sodium cacodylate buffer, the specimens were gradually dehydrated over several hours into 100 % ethanol. The specimens were critical-point dried through liquid CO_2 replacement of ethanol over several purging cycles, followed by heating to reach the critical point for converting CO_2 liquid to gas, using a Leica EM CPD300 instrument (Leica, Wetzlar, Germany).

Critical point-dried samples of each genotype from each time point were imaged using a Zeiss Xradia Versa 520 (Carl Zeiss, Oberkochen, Germany) X-ray microscope (μCT). Samples were immobilized within the narrowing walls of plastic 100 μL micropipette tips. μCT imaging of the Achilles tendon insertion site into the calcaneus was performed using a 4× objective lens, an 80 kV source voltage, and an exposure time of 5 s per projection. Source-sample and sample-detector distances were optimized for phase contrast and for resolutions of about 1 μm/pixel with no binning. An additional scan of the Achilles tendon insertion was done for the 3.5-month and 14-month time points at 0.5 μm/pixel. MicroCT of the midsubstance region more proximally in the Achilles tendons of 7-month-old WT and *Hyp* mice was completed using similar settings. Because of the size of the calcifying sites observed in the midsubstance tendon, two vertical scans were completed in sequence and digitally stitched together for the specimens, allowing for high resolution to be maintained over twice the volume size. Additional conventional radiography was performed on the midsubstance Achilles tendon of WT and *Hyp* mice using a Kubtec Xpert 80 (KUB Technologies, Stratford, CT, USA) operating at 21 kV and at 4× magnification (Fig. S1).

2.3.2. μCT analysis (X-ray microscopy, high resolution)

Structural analysis of fibrocartilage and mineral lacunae of fibrochondrocytes in the Achilles enthesis was completed by cropping to small volumes that included only the calcified fibrocartilage (CF) zone (above the bone cement line), and below the lower grayscale uncalcified fibrocartilage (UF). For each cropped specimen volume, the Otsu algorithm [43] was applied to obtain a collective "semantic" segmentation of mineral lacunae, followed by multiregion of interest (multi-ROI) operation using Dragonfly software 2021.3 (Object Research Systems Inc., Montreal, QC, Canada), resulting in an "instance segmentation" of individual lacunae. The multi-ROI was refined to eliminate the instances the size and morphology that were inconsistent with individual lacunae or represented several connected lacunae. A watershed transform operation was then completed to label individual lacunae of fibrochondrocytes. Next, partial lacunae at the edges of the 3D volume were removed using a peripheral box and a Boolean NAND operation, all in the Dragonfly software. A round of manual assessment through labels of each specimen was completed to eliminate only a few lacunae that were mislabeled by the software. Finally, segmented lacunae of the calcified fibrocartilage zone (150–250 for each specimen) were labeled and color-coded for visualization and quantification. Mineralized volume fractions (MV/TV; MV, mineralized tissue volume; TV, total tissue volume) for the bone-enthesis complex and midsubstance Achilles tendon calcified regions were calculated from 3D segmentations of mineral volume (using deep learning, see below Section 2.4.2). Using a convex-hull or fill operation for each enthesis-bone and tendon mineral segmentation,

respectively, which delineate the periphery and completely fill the interior, the tissue volume (TV) was defined. Circular cross-sectional insets of tendon calcification maps for MV/TV were created using the MV and TV in the Dragonfly bone analysis plugin; for details see [44].

2.4. FIB-SEM serial-surface-view (slice-and-view) imaging

2.4.1. Sample preparation and imaging

Additional hindlimb specimens of WT and *Hyp* mice at 2 months, 3.5 month and 8 months of age were dissected as previously described and fixed in 2 % paraformaldehyde in a solution of 0.1 M sodium cacodylate buffer (pH 7.3) for 2 h at room temperature under constant rotation, then overnight at 4 °C. Specimens were stained with alcian blue (Sigma Aldrich, St. Louis, MO, USA) at pH 5.8 for 4 h before a secondary overnight fixation in 4 % glutaraldehyde. After several washes in sodium cacodylate buffer, the undecalcified specimens were stained by repetitive exposures to osmium tetroxide (Electron Microscopy Sciences, Hatfield, PA, USA) and thiocarbohydrazide (Sigma Aldrich) ligand, as termed the OTOTO method [45,46]. Specimens were gradually dehydrated over several hours into 100 % acetone, followed by epoxy resin infiltration over several days using a decreasing acetone-to-Epon (Electron Microscopy Sciences) ratio, with final embedding in pure Epon polymerized over 2 days at 60 °C. Cured Epon blocks were manually trimmed, sectioned on a microtome, and sections were stained on glass slides for light microscopy using silver nitrate/von Kossa staining for mineral, and toluidine blue for counterstaining. Regions of interest from these light microscopy survey sections were selected in the sagittal aspect of the Achilles tendon insertion site. Corresponding blockfaces were further trimmed and sputter-coated with platinum to provide a conductive 5 nm film on the specimen for additional viewing by SEM (see below Section 2.5) for FIB-SEM region of interest selection.

Tomography at the nanoscale of the Achilles enthesis was performed using backscattered electron (BSE) imaging in a dual-beam Zeiss Crossbeam 520 FIB-SEM electron microscope, operating in its serial-surface-view mode at a probe current of 0.70 nA and at 2 kV imaging voltage after blockface milling in the microscope using a focused ion beam of gallium. Each region of interest for FIB-SEM characterization was chosen such that it included regions of both calcified fibrocartilage and uncalcified fibrocartilage, this ensuring capture of early mineralization events at the mineralization front, as well as including surrounding neighboring soft tissue and fibrochondrocytes. Volumes of the enthesis from both WT and *Hyp* mice were obtained at either 17 nm (15,000–18,000 μm^3) or 5 nm (250–500 μm^3) isotropic voxel size. For the ectopic calcification of the midsubstance region of the Achilles tendon proper, imaging was performed using an FEI Helios Nanolab 660 DualBeam FIB-SEM (Thermo Fisher Scientific) microscope operating at 2 kV imaging voltage, 0.79 nA milling current, and 16 nm voxel size. Nanotomography of additional lamellar bone volumes was carried out as previously described in Buss et al., 2020 [24] also using the FEI Helios FIB-SEM microscope operating under equivalent conditions (at 16 nm and 4 nm voxel size), and likewise using BSE detection.

2.4.2. Deep learning-assisted feature segmentation and analysis (Dragonfly software)

Mineralized regions and structures were segmented using the deep-learning engine in Dragonfly software (Object Research Systems Inc., Montreal). As opposed to threshold-based segmentation, in deep learning, neural networks containing multiple layers are used for image feature recognition and accurate labeling based on the local context of pixel patterns (patterns of patterns) [47]. As a general rule, what a human eye can see, but a human hand would take too long to trace and annotate objectively, a deep neural net can be used for fast and accurate feature segmentation, and we applied this here. For segmentation of close-packed individual mineral tesselles [24], the narrow and irregular boundaries having lower grayscale values were manually traced and excluded from the tesselle semantic segmentation on three 2D images,

and that was the "ground truth" training set. Using a convolutional neural network (CNN) with U-Net architecture having a depth of 5 layers with 64 convolutional filters in the first layer (doubled in each subsequent layer), the pairs of unmodified grayscale input and manually segmented output were partitioned into learning and validation subsets (80 % and 20 %) with 2 iterations of vertical and horizontal data augmentation [47]. The training hyperparameters used were patch size of 64 pixel, batch size of 64, 50 epochs, or until training improvement had not been demonstrated for 10 consecutive epochs. After one cycle of training, a larger selection of 2D images was segmented by the U-Net, and the output required minimal manual touch-up around mineral tesselle boundaries. Because of the propensity of mineralized tissue samples to charge under the electron beam, extreme care was needed to not only train the network to recognize narrow boundaries of lower grayscale values, but also to exclude charging artifacts. That corrected input-output pair comprised the second training set for the same U-Net with the same hyperparameters, resulting in satisfactory segmentation accuracy. To easily create a robust inventory of training examples for fibrochondrocytes, the "snap" tool was used in combination with some manual ROI painter brush corrections in Dragonfly. To assess the bulk of mineralization (as in semantic segmentation), volume thickness maps were constructed. Each semantic segmentation of the mineral in calcified fibrocartilage was smoothed slightly and to the same degree (kernel 3) to reduce computational time. The volume thickness mapping plugin inscribes spheres of maximal diameters at every point within the 3D foreground features. Sphere diameters were color coded using the perceptually uniform "linear" color map [48].

2.4.3. Mineral tesselle labeling and analysis

To label individual mineral tesselles (geometrically approximating prolate ellipsoids) that collectively form the crossfibrillar mineral tessellation pattern and which have narrow and irregular boundaries between tesselles, we used a watershed transform operation in Dragonfly. First, the semantic segmentation of mineral in calcified fibrocartilage images was copied and inverted such that the tesselle boundaries became the foreground. For this inverted ROI, a distance map was constructed which plots and color-codes the distance from every background voxel to the nearest foreground voxel (boundary). Applying the range tool to select the highest intensity areas on the 3D distance map (i.e., the sites most remote from the foreground, corresponding to the centers of the tesselles), so-called "seeds" were then generated as a set of digitally disconnected small objects, and converted into a multi-ROI (instance segmentation). Inputs for the watershed transform were the following: new multi-ROI ("seeds"), the distance map itself with values intensities inverted ("landscape"), and the original semantic segmentation tesselle ROI ("mask"). Several iterations of labeling were tested to find the best intensity range threshold that would label the seeds accurately, with minimal omission of small seeds or fusion of large seeds. In the resultant instant segmentation, tesselles were color-coded using the 64 discrete look-up table, and multi-ROI quantitative analysis was conducted for volume, aspect ratio, and Feret diameters.

2.4.4. Mineral foci analysis

From the 3D images of Achilles tendon insertion with the 5 nm voxel size and lamellar bone images of the same voxel size from our prior study (250–500 μm^3), mineral entities were semantically segmented as described above. Next, a multi-ROI was created, and from this a new ROI was established to then only include digitally isolated mineral entities (foci and immature tesselles), since mature tesselles always digitally connect despite visually distinct boundaries. A distance map was then generated plotting nearest neighbor distances for each background voxel to the nearest foreground voxel. The distribution of these distances was then plotted. A watershed transform was then completed for each volume based on the distance maps, with no mask. This operation creates multicolored labels for all digitally expanded foci that now abut

their digitally expanded neighbors, in a manner resembling a Voronoi tessellation, in 3D [49].

2.5. SEM blockface and TEM imaging

Hindlimbs from older (12–14 months) WT and *Hyp* mice were dissected and fixed as described previously in Section 2.3. In this case, undecalcified specimens were washed and stained in 4 % potassium ferrocyanide-reduced osmium tetroxide. Graded dehydration to 100 % acetone and infiltration and embedding into Epon resin was completed as previously described above. Following microtoming and staining for light microscopy for region selection as above, blocks were sputter-coated with 5 nm Pt and imaged by BSE detection using an FEI Quanta 450 FE-SEM microscope operating at an accelerating voltage of 10 kV. Blocks were then further trimmed, and 80-nm-thick sections were produced on an ultramicrotome, placed on TEM mesh copper grids, and conventionally stained with uranyl acetate and lead citrate. TEM imaging was performed using a Talos F200X S/TEM microscope (Thermo Fisher Scientific) equipped with a 4 k × 4 k Ceta 16 M CMOS camera and operating at 200 kV with an inserted 40 μm objective aperture.

2.6. Immunohistochemistry

Hindlimbs from WT and *Hyp* mice at 3.5 (for enthesis) and 12 (for tendon) months of age were dissected and fixed as previously described in Section 2.3, but using a lower 0.1 % glutaraldehyde concentration in the fixative solution. Specimens were then demineralized in 8 % EDTA containing 0.1 % glutaraldehyde for approximately 4 weeks at 4 °C in a large beaker under gentle stirring (solution was changed once at 2 weeks). Specimens were embedded in paraffin and sectioned onto glass slides with a microtome, and the sections were then deparaffinized with xylene and rehydrated to water through a graded ethanol series. Endogenous peroxidase activity was quenched using a 3 % H_2O_2 solution. Immunohistochemical staining was carried out with an avidin-biotinylated peroxidase enzyme complex-based kit (Vectastain® Universal Elite ABC Kit; Vector Laboratories, Newark, CA, USA) and 3-amino-9-ethylcarbazole substrate (ImmPACT™ AEC Peroxidase Substrate; Vector Laboratories). Anti-PHEX labeling was conducted using a polyclonal antiserum as described in Ecarot and Desbarats (1999) as "a polyclonal antiserum raised in rabbits against a synthetic peptide (CGG) PRNSTMNRGADS corresponding to residues 734-745 of the carboxy-terminal sequence of Phex" (dilution 1:200 in blocking buffer) [50]. Goat anti-mouse OPN (AF808; R&D Systems, Minneapolis, MN, USA) was used as a primary antibody for labeling of similarly cut sections, also diluted 1:200 in blocking buffer. Negative controls consisted of the same procedures while omitting the primary antibody. Hematoxylin counterstaining was applied followed by coverslipping in DAKO Ultramount (reagents from Agilent Technologies, Santa Clara, CA, USA).

3. Results

Here we describe the spatial and temporal mineralization patterns in the Achilles enthesis (physiologic) and Achilles tendon (age-related) under normal (WT) and aberrant regulation (*Hyp*), and we compare these findings to the mineralization pattern for lamellar bone of WT and *Hyp* mice, as reported in 2020 by Buss et al. [24] where the crossfibrillar mineral tessellation was first described and quantified.

3.1. Crossfibrillar mineral tessellation in normal (WT) mouse Achilles enthesis calcified fibrocartilage

3.1.1. Normal enthesis mineral tessellation in comparison to that of normal lamellar bone

Nano- and microscale structural relationships between mineral and the organic extracellular matrix underlie their mechanical performance across larger scales. To examine such structural patterns arising from

cumulative mineralization events, we used multiscale imaging methods (light microscopy, high-resolution X-ray micro-computed tomography [X-ray microscopy], FIB-SEM serial-surface-view tomography, blockface SEM in BSE detection mode, and TEM) to provide correlative 2D and 3D structural information on the Achilles enthesis (Fig. 1A-D).

Using 3D FIB-SEM imaging coupled with deep learning-based segmentation, the 3D organization of mineral was visualized at the mineralization front within the calcified fibrocartilage of the Achilles tendon insertion site (Fig. 1B and Supp. Movie SM1A-WT; light gray – raw data, blue – segmentation, and multicolored – watershed labeling). Starting at the mineralization front (MF) where uncalcified fibrocartilage (UF) transitions into calcified fibrocartilage (CF) (Fig. 1B,C) and then continuing throughout the calcified fibrocartilage, there exists a peculiar space-filling mineral packing pattern, very similar to one observed previously in bone [24] and termed crossfibrillar mineral tessellation. This mineralization pattern for both the enthesis CF examined here, and lamellar bone analyzed previously, consists of close-packed mineral tesselles (geometrically approaching prolate ellipsoids) having narrow and irregular boundaries that are less electron-dense. These boundaries between the mineral tesselles range in thickness from tens to hundreds of nanometers and are clearly visible in original micrographs (without segmentation). While some tesselles appeared to blend with their neighbors for short segments of their boundaries, in general the less-mineralized boundaries were consistently present throughout the entirety of the calcified fibrocartilage extending from the mineralization front to the cement plane (Fig. 2A). At the scale of several micrometers and larger, we failed to observe widespread fusion or "sintering" of tesselles into solid mineral volumes without organic gaps [51].

3.1.2. Tesselle size and expansion from small mineral foci

Comparing measurements from two FIB-SEM volumes (Fig. 1D) – one from below the mineralization front of the calcified fibrocartilage (Figs. 1B,C and 2B, and Supp. Movie SM2A-WTA–SM2C-WT), and one from below the mineralization front of lamellar bone [24] (shown in Fig. 2B) – a similar distribution of tesselle aspect ratios was observed (Fig. 1D). In both cases, starting at or near the mineralization front as viewed by SEM-BSE or FIB-SEM tomography, small mineralization foci within uncalcified fibrocartilage or bone osteoid expand to form space-filling mineral tesselles in 3D (Fig. 2A,B and Supp. Movie SM1A-WT). Using the watershed labeling function of the software applied to complete tesselles (Fig. 2B, incomplete tesselles at the margins were digitally removed), we computed the overall distribution of tesselle equatorial widths (the minimum Feret diameter) that generally aligns perpendicular to the long axes of both the tesselles and the collagen fibrils. Taken together, these 3D FIB-SEM tomography data (Fig. 2B) over small volumes of fibrocartilage, coupled with SEM backscattered imaging over much larger 2D block faces (Fig. 2A), indicate a greater size variation of tesselle sizes and heterogeneity in tesselle spacing/packing in fibrocartilage as compared to that found in mouse circumferential lamellar bone.

We next considered whether the larger and more heterogeneously sized and spaced mineral tesselles in fibrocartilage (in comparison to bone) originate primarily from more sparsely and irregularly positioned discrete nanometer-scale mineral foci, or alternatively, whether fusion of mineral volumes at or near the mineralization front contribute to tesselle dimensions. To investigate this question, we calculated the distribution of nearest-neighbor distances of segmented mineral foci near the mineralization fronts of fibrocartilage and bone using higher-resolution FIB-SEM volumes acquired at 5 nm voxel sizes or less (sufficient to resolve mineral foci). For lamellar bone, the distance
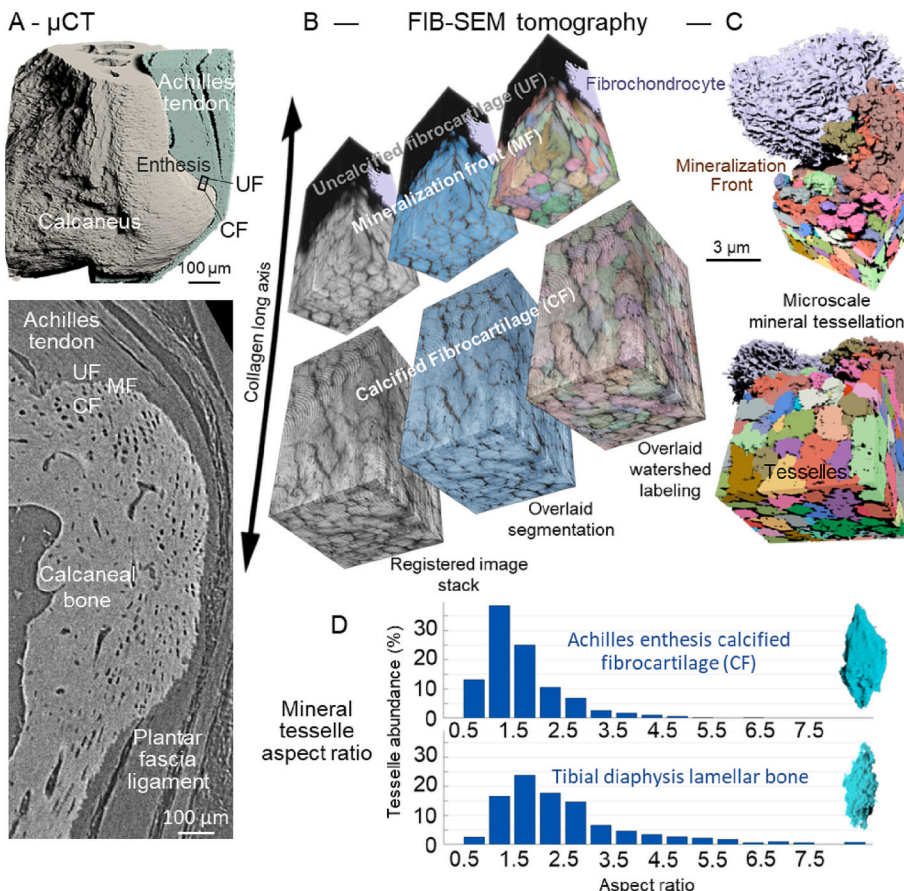

Fig. 1. Wildtype mouse Achilles enthesis insertion and crossfibrillar mineral tessellation of calcified fibrocartilage at the mineralization front. (**A**) MicroCT segmentation (top panel) and 2D sagittal projection (bottom panel) of mouse Achilles tendon and plantar fascia ligament insertion sites at the superior and inferior calcaneal tuberosities, respectively. The enthesis has zones of uncalcified fibrocartilage (UF) and calcified fibrocartilage (CF). (**B, C**) Electron microscopy (FIB-SEM Serial-Surface-View) tomographic 3D reconstruction, segmentation, and watershed labeling reveals micrometer-sized, close-packed, space-filling mineral tesselles commencing at the mineralization front of normal mouse Achilles enthesis fibrocartilage. Panel C shows labeled (colored) mineral tesselles in relation to a fibrochondrocyte positioned at the mineralization front (unmineralized collagen digitally removed). (**D**) Distribution of mineral tesselle sizes generated from watershed labeling in Achilles enthesis fibrocartilage (and, for comparison, in lamellar bone likewise near the mineralization front) obtained from FIB-SEM mineralized tissue volumes. An example of a typical tesselle from each volume, representing their general morphological characteristics (as geometrically approximating prolate ellipsoids) is shown to the right (in turquoise). A, 7-month-old WT; B-D, 2-month-old WT. (For interpretation of the references to color in this figure legend, the reader is referred to the web version of this article.)
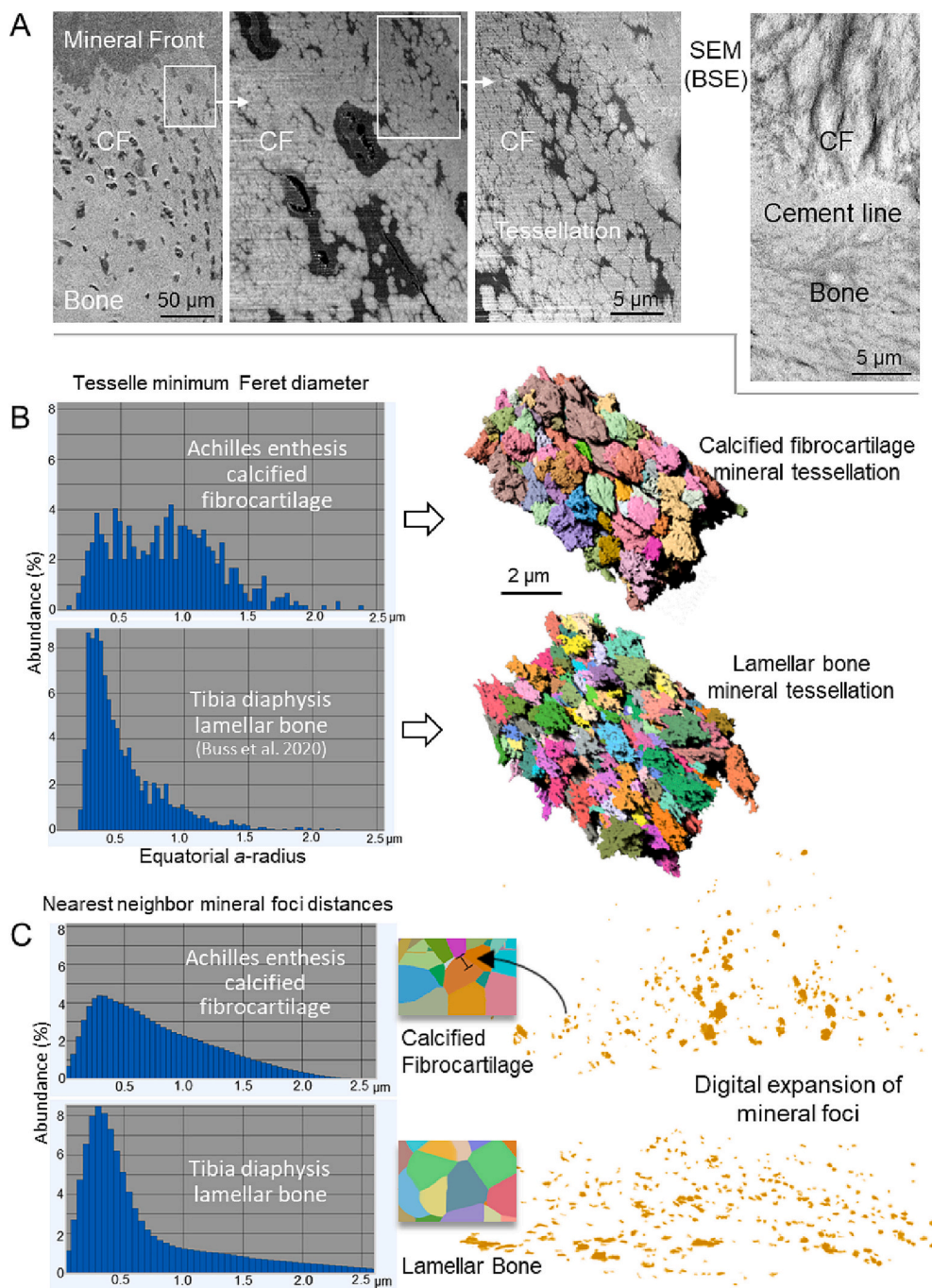
Fig. 2. Wildtype mouse crossfibrillar mineral tessellation in fibrocartilage compared to bone. (**A**) An increasing magnification series of polished block faces containing the Achilles enthesis calcified fibrocartilage (CF) zone as viewed by SEM backscattered electron imaging (SEM-BSE) to highlight mineral shows the distribution of mineral tesselles in 2D that continue to the cement line interfacing with bone. Note the larger size of the mineral tesselles in fibrocartilage compared to bone. (**B**) Distribution of minimum equatorial diameters of watershed-labeled tesselles (left panels) as measured from 3D FIB-SEM segmented volumes (right panels) of mineral-tessellated calcified fibrocartilage and lamellar bone (for comparison). (**C**) Distribution of nearest-neighbor distances (indicated by bracket for one mineral focus), then plotted for all foci in the corresponding histogram of immature mineral foci from above the mineralization front as labeled/segmented from FIB-SEM volumes. These distances represent a digital, simulated expansion of mineral foci (represented by the bracket in the associated Voronoi partition). A, 2-month-old WT; B, 2-month-old (calcified fibrocartilage) and 3.5-month-old (bone); C, 2-month-old calcified fibrocartilage and bone.

distribution was unimodal and centered around 0.35 μm (Fig. 2C). This value represents the modal "radius" at which another expanded mineral focus would be met in a Voronoi pattern; therefore, the modal diameter of each digitally expanded focus would be 0.7 μm for bone. This 0.7 μm value approximates that which we have observed as the minor axis (minimum Feret diameter) after natural tesselle growth (Fig. 2B), and moreover, it suggests that individual mineral foci are indeed primary "seeds" that expand to become mineral tesselles. In Achilles enthesis calcified fibrocartilage, a similar effect was observed, although with a wider distribution of sizes in both the distribution of mineral foci nearest-neighbor distances and the minor *a*-axis of mature tesselles. This indicates that a greater sparsity and irregularity of initial foci formation determines mature tesselle morphology (Fig. 2B).

3.1.3. Observations on 3D volume-filling mineral tessellation and the tesselle boundaries

To assess the packing pattern of mineral tesselles at finer scales, and thus the relationship of mineral nanocrystals within and between collagen fibrils at the periphery of individual tesselles found in the enthesis fibrocartilage, we completed a manual segmentation from a 5 nm voxel resolution volume (Fig. 3A,B). At each tesselle boundary there existed a less-electron dense (a less-mineralized) region ranging in thickness from tens to hundreds of nanometers. This was a consistent feature over all samples and in mice of all ages, indicating these boundary zones generally persist over time in calcified fibrocartilage (that is not remodeled, in contrast to bone). As viewed in FIB-SEM images, within the tesselles, mineral texture shows clear evidence of integrating with the underlying banding pattern of collagen fibrils
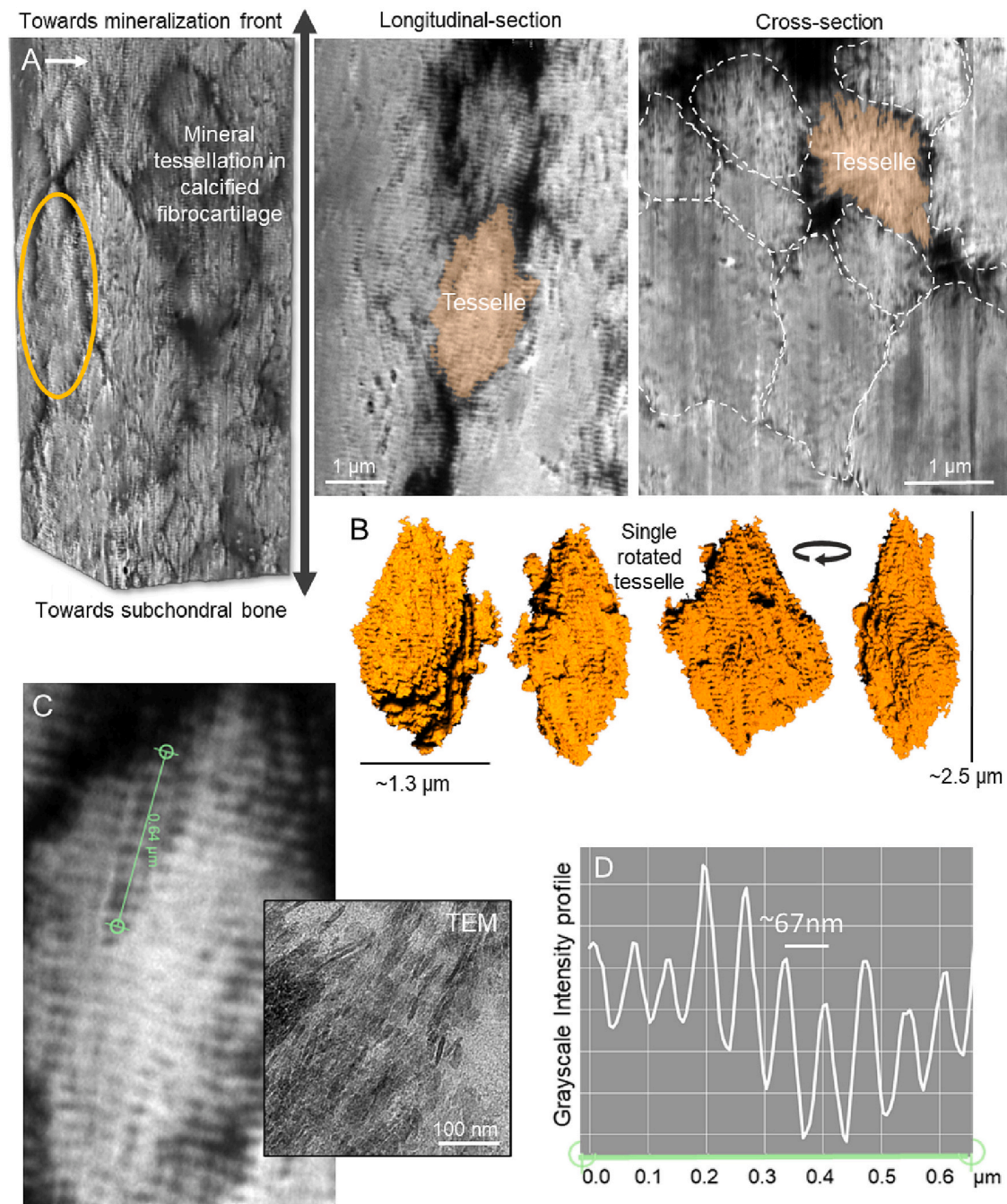
Fig. 3. High-resolution imaging of crossfibrillar mineral tessellation in WT mouse Achilles enthesis calcified fibrocartilage. High-resolution rotation images of an individual tesselle (orange) from within 10 μm below the mineralization front. (**A**) A region from a FIB-SEM stack showing how tesselles interface with one another leaving nanoscale intervening gaps of unmineralized organic matrix at their boundaries. Different projections of the same tesselle are shown in the three panels showing longitudinal and cross-sectional views. Dashed lines demarcate neighboring individual tesselles. (**B**) The same segmented tesselle (as in the A panels) in rotation with surrounding tissue digitally removed. Underlying collagen fibril molecular striation patterns (banding pattern) are reflected in the mineral segmentations. (**C**) Single 2D image slice from the sampled volume of the same tesselle showing preferential mineralization along the collagen molecular spacing, likewise imaged by TEM (from a different tesselle) showing how this pattern originates from the distribution of individual nanocrystals related to the collagen fibril. (**D**) Intensity profile of the grayscale values along the green line indicated in panel C shows 10 crests and troughs. Samples from 8.5-month-old mice except TEM image from a 12-month-old mouse. (For interpretation of the references to color in this figure legend, the reader is referred to the web version of this article.)

(Fig. 3A,B, and left panel in C). In other samples imaged by TEM (Fig. 3C, right panel), a similar pattern was observed where mineral crystals aligned with the gap/overlap molecular spacing of the collagen fibrils observed as the well-known characteristic 67 nm repeat pattern (Fig. 3D).

3.2. Crossfibrillar mineral tessellation in Achilles enthesis calcified fibrocartilage in the Hyp mouse model of XLH

Based on the incidence of calcifying enthesopathy in XLH, here we also aimed to gain a greater understanding of Achilles enthesis structure in *Hyp* mice. First, like for WT mice as described above, we imaged *Hyp* Achilles enthesis insertions at different mouse ages using X-ray micro-

computed tomography (µCT, X-ray microscopy). Compared to normal WT mice, *Hyp* mice presented with a substantially decreased mineral volume fraction and increased bone porosity in the calcaneus in the vicinity of the Achilles tendon insertion site, readily evident in *Hyp* mice at all the ages we examined (from 3.5 months to 14 months, Fig. 4A and Supp. Movies SM4A, SM4B, SM5A). Although some small calcaneal enthesophytes were observed at the Achilles enthesis, large enthesophytes were not consistently noted at this site (even in older mice), but sometimes they were more pronounced on the plantar fascia side of the calcaneus, but only slightly so (Supp. Movie SM4B provides a good example).

Given that hallmark peri-osteocytic lesions (POLs, halos) in bone are a characteristic feature of XLH/*Hyp* – where osteocyte mineral lacunar volumes are enlarged [52] – we investigated whether this might likewise occur related to fibrochondrocyte mineral lacunar volumes in the calcified fibrocartilage. To assess this, 3D full-volume fibrochondrocyte mineral lacunae were segmented at the insertion site from WT and *Hyp* mice using watershed transform labeling (Fig. 4B). We use the term "mineral lacuna" as previously described [52] to specify the combined

space occupied by a cell and any surrounding unmineralized matrix, as this is what is detected using µCT. Using this same methodology of assessment as we used for bone, no significant changes in fibrochondrocyte mineral lacunar volumes were observed either within WT or *Hyp* mice of different ages, or between WT and *Hyp* age-matched mice ranging from 3.5 months to 14 months of age (Fig. 4B, C).

For further analysis of enthesis sites, SEM backscattered electron (BSE) imaging – that highlights mineral – was performed on calcaneal Achilles enthesis and plantar fascia enthesis on the block faces of Epon-embedded and microtomed samples (Fig. 5A). Using this imaging method, additional details on mineral distribution were observed; for example, in WT mice, the highly interdigitated interface of the calcified fibrocartilage was observed with the underlying calcaneal bone, and fibrochondrocyte mineral lacunae and distribution were readily apparent. This broad survey method of the blockface amongst samples was useful for comparisons to show the less-organized distribution of fibrochondrocytes/mineral lacunae in the *Hyp* mice versus the WT mice. It also revealed thin "rings" of mineral surrounding fibrochondrocytes in the *Hyp* mice on the plantar fascia side of the calcaneus, perhaps an early
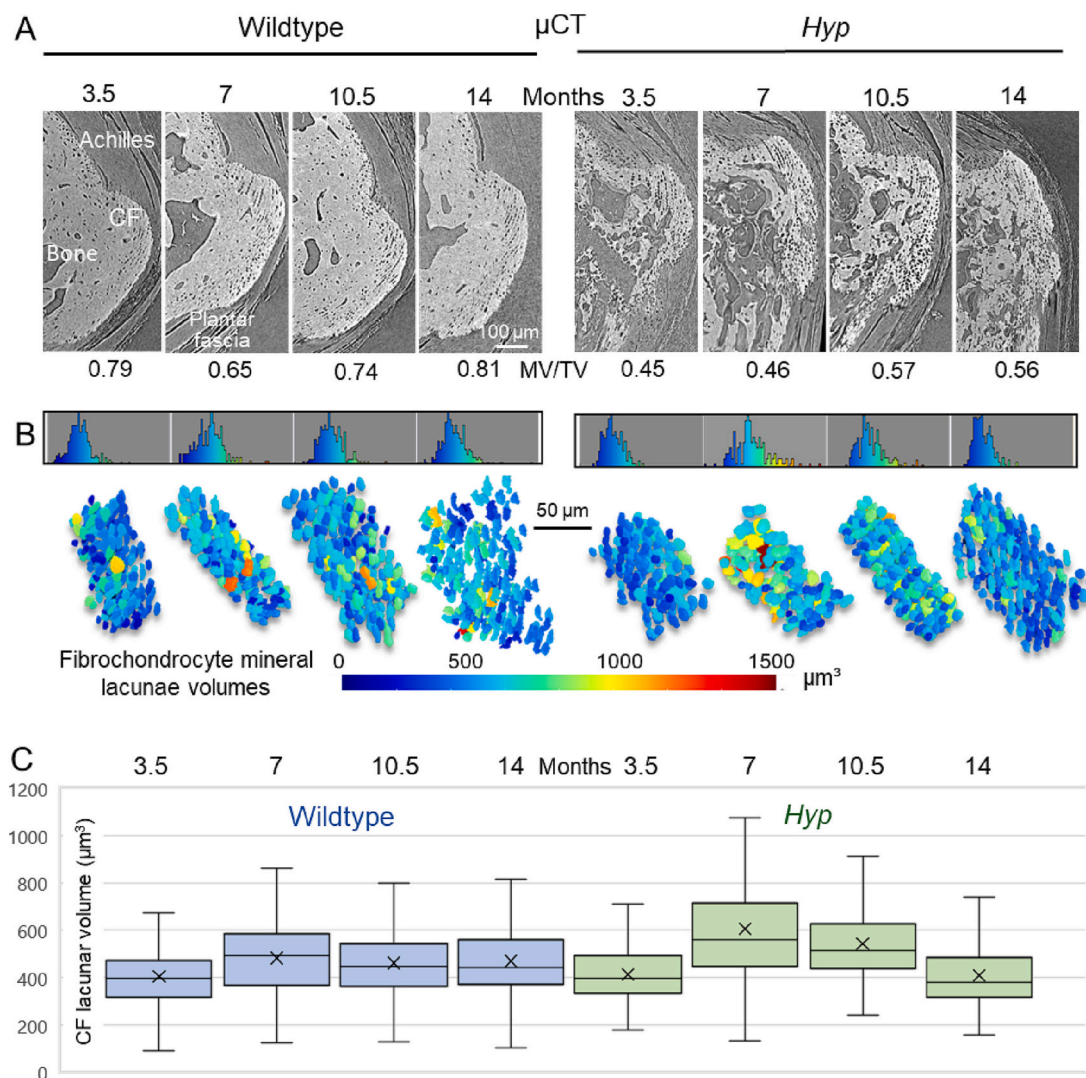

Fig. 4. MicroCT of Achilles and plantar fascia insertion sites in WT and *Hyp* mice. (**A**) MicroCT sagittal single 2D projections from mice of various ages as indicated. CF indicates calcified fibrocartilage. *Hyp* calcaneal bone and calcified fibrocartilage show extensive hypomineralization showing as decreased mineralized tissue volume fraction (MV/TV) at this level of magnification across each age. Enthesophytes are not prominent in the sampled entheses. (**B, C**) Fibrochondrocyte mineral lacunae volume analysis in Achilles enthesis calcified fibrocartilage obtained through watershed transform labeling, color-coded heat-mapping of their distribution, and plotting and comparison of lacunar volumes. No differences in lacunar volumes were determined within and between the mouse ages and the phenotypes. For each plotted box, the central line of the box represents the median, the "x" the mean, the bottom and top lines of the box the median of the first and third quartiles, and the whisker arms extend to the overall maximum and minimum values. MV, mineralized tissue volume; TV, total tissue volume.
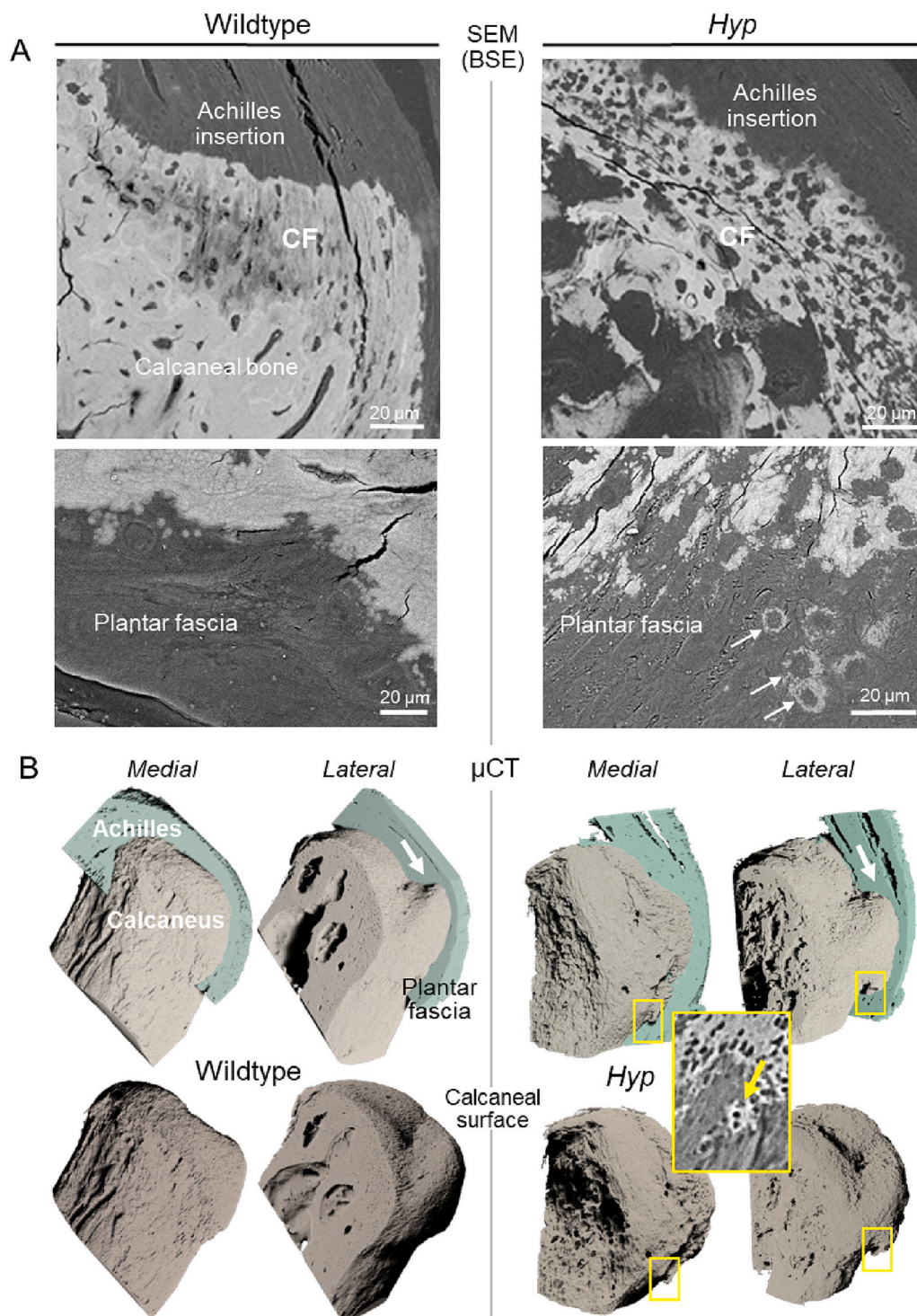
Fig. 5. Achilles and plantar fascia entheses in WT and *Hyp* mice. Correlation of insertion-site structure using electron (SEM) and X-ray (μCT) imaging. (**A**) SEM-backscattered electron imaging (SEM-BSE) of embedded-sample block faces from WT and *Hyp* 12-month-old mice showing evidence of irregular morphology and deficient mineralization at insertion sites in the *Hyp* mice. Arrows indicate unusual circular/spherical mineral deposition around fibrochondrocytes in the deeper regions of the uncalcified cartilage zone, perhaps the beginning of an enthesophyte. (**B**) MicroCT segmentations from different mice of nearly the same age (here 10.5 months old) show an expansion of calcified fibrocartilage within the plantar fascia insertion (yellow frames). The top panels show an Achilles tendon segmentation (green) at a partial cut-away plane, and the bottom panels show mineralized tissue only (bone/calcified fibrocartilage). (For interpretation of the references to color in this figure legend, the reader is referred to the web version of this article.)

mineralization event (Fig. 5A, arrows). Such observations were placed in broader context when localized at a larger scale using 3D re-constructions from μCT analyses of both entheses of the calcaneus that were examined in both mouse phenotypes (Fig. 5B). 3D-rendered surface features shown in μCT movies (Supp. Movie SM5A) reveal morphological differences between the insertion sites of WT and *Hyp* in 10.5-month-old mice, with the mineralized *Hyp* enthesis and bone surfaces showing increased surface roughness.

3.3. 3D nano- and microstructure of the mineralization front of Achilles enthesis calcified fibrocartilage in WT and Hyp mice

3.3.1. Hyp mice display defective calcified enthesis fibrocartilage structure as early as 2 months of age

Previously we described in 3D that *Hyp* mice have defective nano- and microstructural organization of mineral within lamellar bone that appears to be normally mineralized when using lower resolution conventional assessment techniques; in particular, *Hyp* mice have bone with incomplete crossfibrillar mineral tessellation that leads to a less-defined mineralization front and a defective tessellation pattern that presumably

at least partly contributes to the *Hyp* macroscopic bone deformities [24]. This type of mineralization defect at the nano- and microscale is unrecognizable by conventional light microscopy and μCT methods, but requires the resolution of 3D electron microscopy methods. To investigate whether the pathogenesis of XLH/*Hyp* involves similar structural malformations of mineral at entheses, we examined in detail and in 3D the mineralization front of the Achilles insertion into the calcified fibrocartilage zone. We assessed multiple FIB-SEM volumes of various ages from WT and *Hyp* mice, starting with a matched pair at 2 months of age (Fig. 6 and Supp. Movies SM6A, SM6B). Enthesophytes were not evident in these 2-month-old mouse samples.

While WT mice displayed a characteristic trajectory of mineralization from small mineral foci tens to hundreds of nanometers in size which then grew preferentially aligned with the long axis of collagen fibrils to form a space-filling assembly with neighboring tesselles, *Hyp* specimens lacked such a mineralization trajectory to produce space-filling mineral tessellation (Supp. Movies SM6A, SM6B). Below the ill-defined *Hyp* mineralization front, this was readily observed in 3D as generally smaller and more irregular and isolated mineral volumes that did not abut against one another and instead had wider unmineralized spaces between them (Fig. 6A–C).

3.3.2. Hyp mice exhibit an aborted and irregular mineral foci growth trajectory in enthesis fibrocartilage

FIB-SEM reconstruction of fibrocartilage volumes at 2-, 3.5- and 8.5-month-old mouse ages demonstrated smaller and more scattered mineral tesselles in *Hyp* mice, and incomplete space-filling (Fig. 6 and Supp. Movies SM6A, SM6B. Specimens of fibrocartilage from 2-month-old WT and *Hyp* mice were additionally compared to other sampled volumes

from older mice by FIB-SEM tomography. To quantify the observations depicted in Fig. 6, we applied thickness mapping to semantic segmentations of mineral (not labeled as individual tesselles) of mineral from each volume (Fig. 7A,B). Using the sphere-fitting algorithm to plot and locally color-code 3D volume thickness of the segmented mineral, when compared to WT mice, *Hyp* mice showed a prevalence of smaller volume thickness values in the calcified fibrocartilage (Fig. 7A). Next, we then selected all of the isolated mineral entities that were not digitally "touching" the mineralization front (i.e. mineral foci), and approximating the mineralization front of the larger attachment site as a 2D cross-sectional planar area, we calculated that from this perspective there were more than double the number of isolated mineral foci in the *Hyp* (7.6 per 10 μm^2) as compared to the WT (3.1 per 10 μm^2) in mouse fibrocartilage (Fig. 7C and Supp. Movie SM7A), this being attributed to the persistence of aborted immature mineral foci over a larger distance in the vicinity of the mineralization front (versus WT where small mineral formations were only observed immediately above the mineralization front). We used area to normalize this measurement because if volume was used it would skew the data given that in WT mineralization there are normally no foci that persist below the mineralization front – this is because at that point foci abruptly transform into space-filling tessellation of geometrically approximating prolate ellipsoidal mineral tesselles. In *Hyp* mice, untessellated mineral foci and ellipsoids persist throughout the volume and there is no clear mineralization front over an extended distance (see Supp. Movie SM7A) – similar to what we have shown in lamellar bone [24].
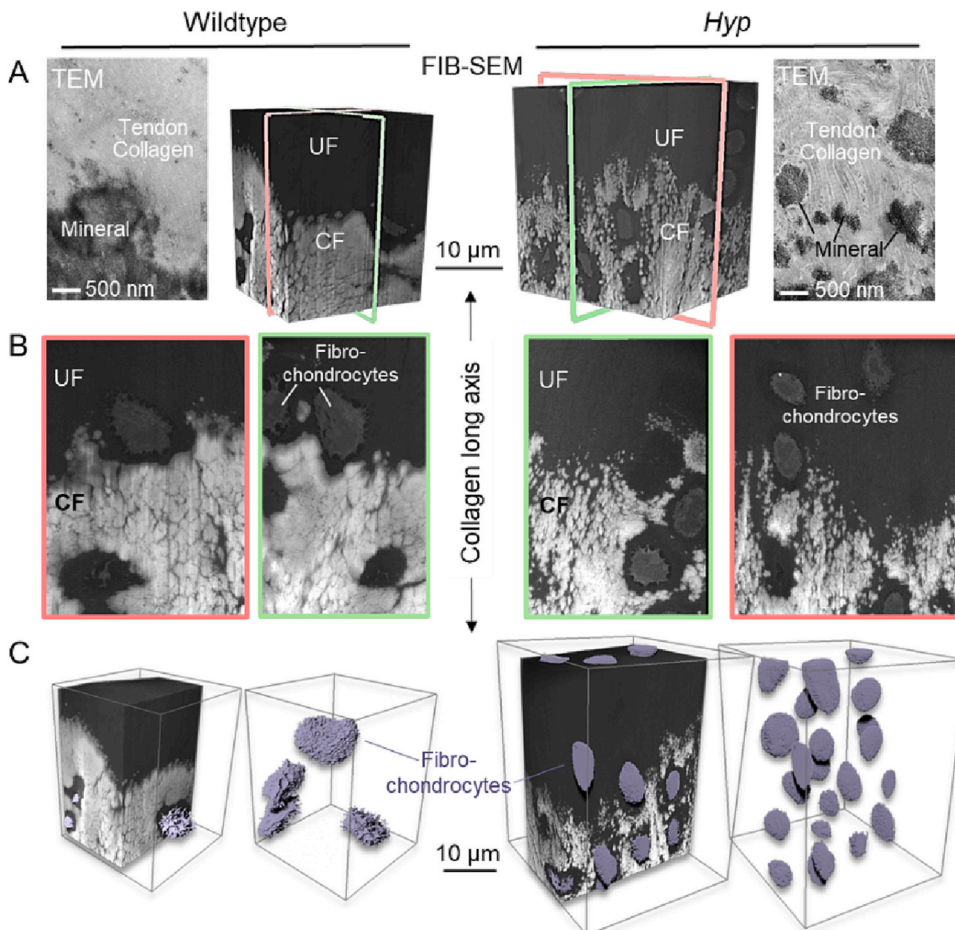

Fig. 6. FIB-SEM tomography 3D reconstructions of 2-month-old WT and *Hyp* mouse Achilles enthesis. (**A**) 3D FIB-SEM volumes and higher-resolution TEM of mineralization events directly adjacent to the mineralization front. (**B**) 2D projections from the inner panels of A showing the extent of mineral packing in normal and *Hyp* mice. (**C**) Additional 3D views showing the location of fibrochondrocytes near the mineralization front (fibrochondrocyte cells only are shown in the right panels, with surrounding tissue being digitally removed). All from mice aged 2-months-old except TEM images (from 12 months).
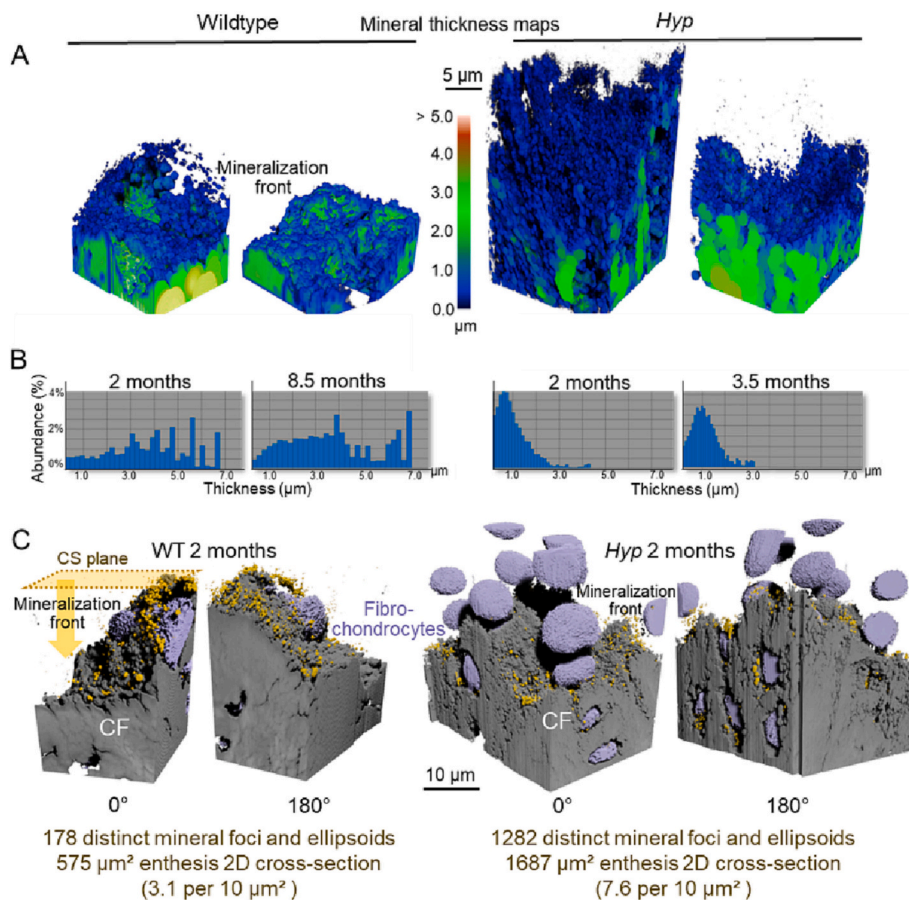
Fig. 7. Comparison of the calcified fibrocartilage mineralization front 3D landscape between WT and *Hyp* mouse Achilles insertion as analyzed by FIB-SEM tomography. (**A, B**) Local volume thickness mapping (A) and mineral thickness abundance (B) throughout 17 nm-voxel FIB-SEM volumes showing a narrower range of mineral volumes indicative of disconnected foci and immature tesselle volumes compared to the close packing of tesselles in WT mice. (**C**) From the 2-month-old age-matched pair, analysis of isolated mineral foci (gold color) above the mineralization front assessed by number in relation to the cross-sectional (CS) area of the mineralization front, illustrates that *Hyp* mice have more scattered, numerous smaller mineral volumes (foci and immature tesselles) than in WT mice, and that a distinct mineralization front is difficult to identify/outline. (For interpretation of the references to color in this figure legend, the reader is referred to the web version of this article.)

3.4. PHEX and osteopontin localization at the Achilles enthesis insertion of WT and Hyp mice

To gain insight into which proteins may contribute to these divergent trajectories of fibrocartilage mineralization, we assessed the presence and location of PHEX and OPN by immunohistochemical staining of WT and *Hyp* enthesis insertion sites (Fig. 8). As has been shown for most mineralized tissues [53], staining for OPN was found to be closely associated with the mineral in the CF of both WT and *Hyp* mice (Fig. 8A, B). The PHEX antibody clearly showed the well-known staining pattern for osteoblasts and osteocytes (and their cell processes) in WT bone (in this case tibial bone located proximally within the same sections), but there was no staining related to WT enthesis fibrochondrocytes (Fig. 8C), this compared to our control incubations (Fig. S2). In *Hyp* mice, there was no staining for PHEX observed in either tibial bone or enthesis fibrocartilage (Fig. 8D), as would be expected as a result of their truncating mutation in PHEX.

3.5. Age-related ectopic calcifying tendinopathy in WT and Hyp mice: 3D ultrastructural aspects and crossfibrillar mineral tessellation

During the course of this study, we fortuitously observed in the μCT scans of the lower hindlimb — dissected to contain the full length of the Achilles tendon — that both older WT and *Hyp* mice consistently had large discrete regions of electron opaque mineral within their tendon midsubstance, occurring well proximal of, and not connected to, the enthesis or enthesophytes (Fig. 9). Given this observation in a highly aligned, collagen fibril-dominated extracellular matrix, we considered whether this age-related occurrence in WT mice of ectopic mineralization might have a mineral tessellation trajectory similar to what was observed in WT and *Hyp* entheses and lamellar bone. In mice over 7

months of age, calcifying Achilles tendinopathy was prominent in every WT and *Hyp* mouse we observed (Fig. 9A–C, Supp. Fig. S1), bilaterally, and in mice of both CD1 and C57BL/6 strain backgrounds. We are unaware of studies that have recognized this frequent occurrence in older mice, and we describe it in detail below. In Achilles midsubstance tendon sections from 12-month-old WT mice, strong osteopontin immunostaining was associated with the ectopic mineralized regions (here decalcified for paraffin embedding and sectioning) of the midsubstance tendon (Fig. 9D, E). By electron microscopy of polished sample block faces imaged by SEM-BSE, a surprising resemblance occurred for the ultrastructural patterning of WT mineral foci and mineral tessellation seen in bone and calcifying fibrocartilage versus the defective patterning and defective tessellation seen in these mineralized tissues in *Hyp* mice (Fig. 9F,G and Supp. Movie SM9A). In *Hyp* mice there were large regions of scattered and isolated foci together with an overall aberrant structure of ectopically calcifying regions (Fig. 9G and Supp. Movie SM9A) as compared to the more organized WT tendon midsubstance calcification pattern having distinct regions such as clear zones of unmineralized collagen, a mineralization front, and a heavily mineralized tessellated zone (Fig. 9F and Supp. Movie SM9A).

In conventionally stained TEM sections of the WT calcifying Achilles tendon midsubstance site, extensive mineralization followed a 3D tessellating pattern both immediately adjacent to and farther away from tenocytes (Fig. 10). Mineralization was observed both between and within the tendon collagen fibrils, with mineral banding patterns being observed (Fig. 10A, C, E). In TEM sections of the *Hyp* calcifying Achilles tendon midsubstance site, scattered mineralization foci (rather than interlocking tesselles) were prominent, with much of the mineralization occurring between the collagen fibrils (Fig. 10B, D, F).

To assess the 3D nano- to microstructure of this ectopic mineralization in normal WT mice, and in a correlative manner, our approach was
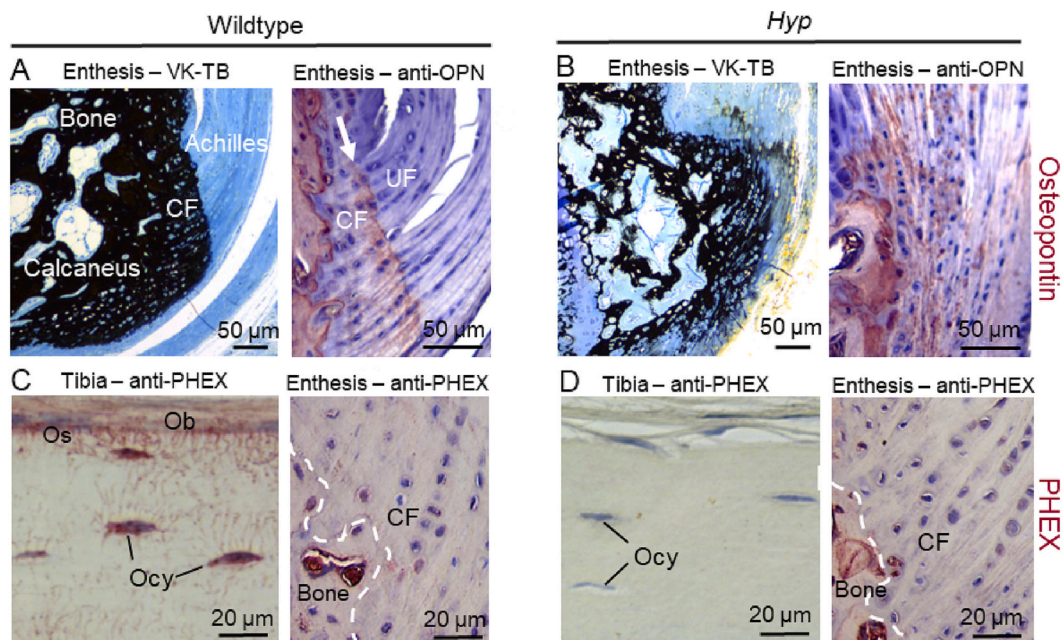
11

Fig. 8. Light microscopy histology and immunostaining for OPN and PHEX at the Achilles insertion in WT and *Hyp* mice. (**A, B**) Staining for mineral (black) using the Von Kossa method (VK) with counterstaining from toluidine blue (TB) on epoxy sections, and immunostaining for osteopontin/OPN (red) on paraffin sections of EDTA-decalcified samples. In WT enthesis, OPN is prominent in the bone and calcified fibrocartilage, and particularly at the mineralization front (arrow) between uncalcified fibrocartilage (UF) and calcified fibrocartilage (CF). In *Hyp* enthesis, the OPN immunostaining pattern is diffuse in the fibrocartilage, reflecting the scattered mineralization pattern that occurs there in *Hyp* mice, with the mineralization front not being well defined. (**C, D**) Comparison of immunohistochemical staining for the PHEX enzyme in decalcified paraffin sections of WT and *Hyp* lamellar bone versus Achilles enthesis calcified fibrocartilage. Whereas WT bone tissue shows prominent immunolabeling for PHEX in osteoblasts (Ob) and osteocytes (Ocy), and in their cell processes (C), *Hyp* mouse bone (lacking the PHEX enzyme) shows the expected lack of immunostaining in the absence of PHEX, as does the *Hyp* enthesis (D). No PHEX immunostaining is observed in the examined entheses of WT mice. VK/TB-stained 2-month-old; Osteopontin and PHEX immunostaining 3.5-month-old. Os, osteoid. (For interpretation of the references to color in this figure legend, the reader is referred to the web version of this article.)

to use the same block from Fig. 9D for SEM-BSE blockface imaging (Fig. 11A–C) followed by subsequent smaller region preparation for FIB-SEM serial-surface-view imaging (Fig. 11D–F). Here we found that mineral tesselles were quite larger in length (up to and exceeding 5 μm). Similar to bone and enthesis fibrocartilage, we observed discrete lower grayscale boundaries around much of each tesselle's periphery. Four tesselles were segmented in 3-dimensions in Fig. 11D (also shown in Supp. Movie SM11A-WT), with corresponding images in different views shown in Fig. 11E, F. Despite the larger tesselle size, close-packing tessellation was achieved as observed in both 2D and 3D imaging (Supp. Movie SM11A-WT).

4. Discussion

Here we describe crossfibrillar mineral tessellation in mouse enthesis fibrocartilage, in Achilles calcifying tendinopathy, and in *Hyp* calcifying enthesopathy. This shared 3D mineralization pattern amongst mineralizing collagen-based extracellular matrices aligns with what we have described for lamellar bone [24], and identifies a common calcification trajectory for mineralized tissues. In this comparative analysis of differently aged mouse mineralized tissues for both WT and *Hyp* mice, we extend our original report on crossfibrillar mineral tessellation in lamellar bone to a comparative 3D analysis of Achilles enthesis structure at the micro- and nanoscale in these two mouse strains using X-ray and electron microscopy and electron tomography methods. Given the distinctive nature of enthesis fibrochondrocytes that produce zones of fibrocartilaginous extracellular matrix that does not, or does, calcify (i.e. commonly called uncalcified fibrocartilage and calcified fibrocartilage), we examined this mineralization pattern in WT mice and compared it to that found in *Hyp* mice. More specifically, we describe 3D features of fibrocartilage mineral at both the microscale and ultrastructural levels

in *Hyp* mice having similar calcifying enthesopathy characteristic of the Achilles enthesis in XLH patients [14,15,26,27,30,33,34]. Furthermore, we identify and characterize an Achilles tendon midsubstance calcifying tendinopathy in both WT and *Hyp* mice.

Enthesis fibrocartilage has evolved with unique properties to minimize stress concentration at a juncture of juxtaposed tissues having a large discrepancy in their elastic moduli. The fibrocartilage enthesis has four zones with distinct compositional and structural properties starting from the tendon or ligament, then to uncalcified fibrocartilage, then across the mineralization front into calcified fibrocartilage, and finally continuing across to a mineralized cement plane interfacing with underlying bone. Even within this continuum of different unmineralized and mineralized extracellular matrices, finer gradients of properties and adaptations within each individual zone have been identified that act to prevent stress singularities, contributed to by features such as collagen fiber orientation, a corrugated mineralization front, and a mineralization gradient [4,17,18,20,54–58]. It is well-known that matrix-mineral (organic-inorganic) relationships as generally found in mineralized tissues are critical determinants underlying their macro-level performance [59–61].

4.1. Nano- to microscale (crossfibrillar mineral tessellation) trajectories of mineralization in WT and Hyp mouse Achilles enthesis

The inherent trade-off between high resolution and broader context traditionally complicates our ability to provide seamless, integrated understanding between magnification scales for characterizing tissue, cell and molecule structural biology. Mineralization of tissues, notably occurring in extracellular matrices, adds yet another dimension to be analyzed and integrated into our understanding — in this case an inorganic phase of calcium-phosphate mineral. However, significant
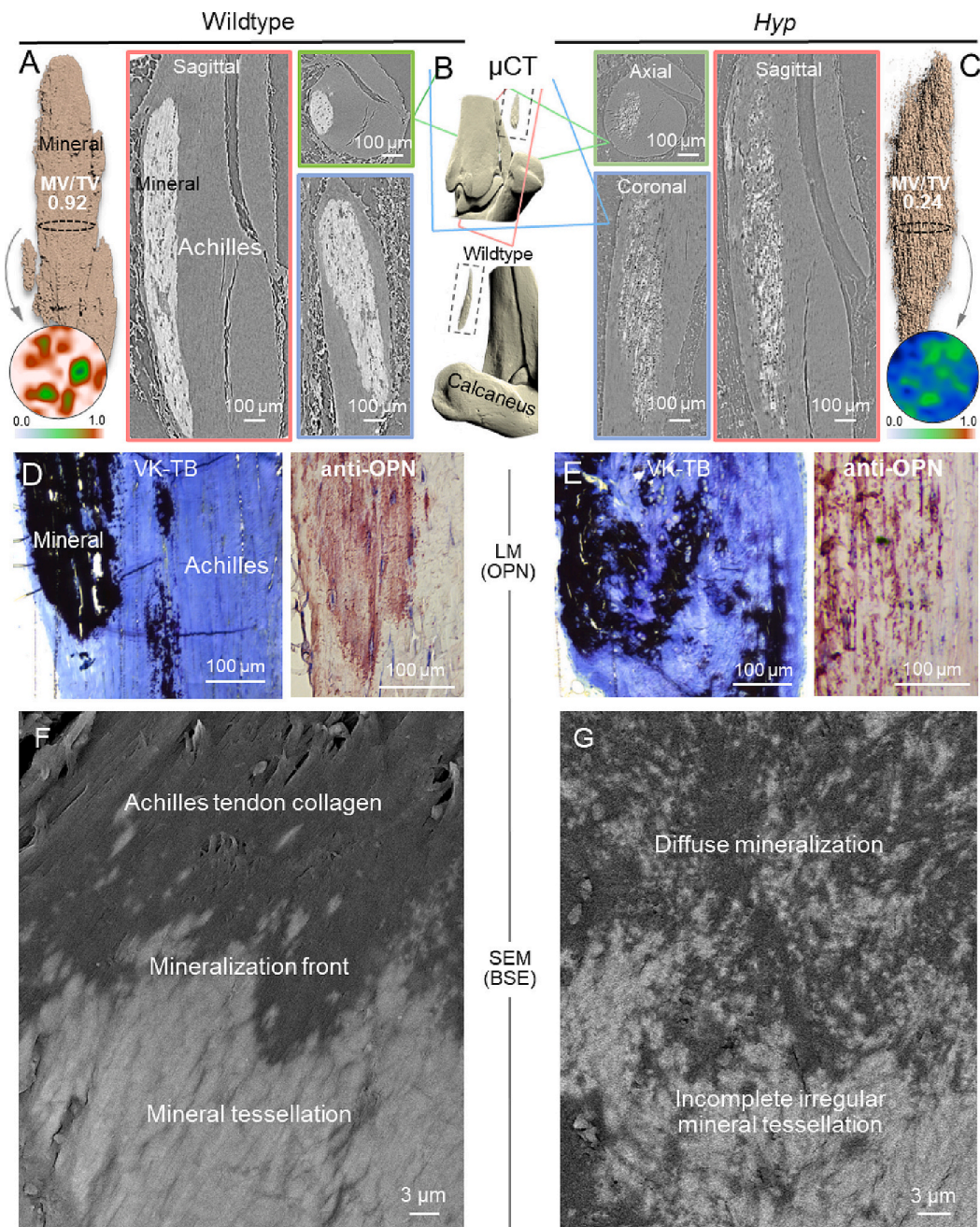
Fig. 9. Multiscale analysis of Achilles tendon midsubstance calcifying tendinopathy in both WT and *Hyp* mice. (**A, C**) Vertically stitched high-resolution μCT projections and 3D segmentation of complete calcifying lesions from the midsubstance Achilles tendon of 7-month-old WT and *Hyp* mice, with a substantially less MV/TV in *Hyp* compared to WT within each calcifying lesion volume (cross-sectional mineral volume fraction maps are shown in circular profile). (**B**) Lower magnification example from a WT mouse showing the general location of midsubstance calcifications (dashed boxes). (**D, E**) Von Kossa (black)/Toluidine Blue staining of mineralized regions, and OPN immunostaining of the midsubstance calcification tissue (here from a similar region from 12-month-old WT and *Hyp* mice). (**F, G**) SEM-backscattered electron imaging (SEM-BSE) of block faces of the midsubstance calcification region in 12-month-old mice, with clear crossfibrillar mineral tessellation in the WT tendon, but with scattered, spotty mineralization in the *Hyp* tendon, observations consistent with *Hyp* bone described previously, and here in the present study with calcifying fibrocartilage at enthesis sites. MV, mineralized tissue volume; TV, total tissue volume. (For interpretation of the references to color in this figure legend, the reader is referred to the web version of this article.)

advances in our knowledge of these tissues have been afforded by microscopy methods appropriate for different magnification scales. Here, for the study of Achilles enthesis structure, we used predominantly X-ray microscopy (μCT with voxel size less than 1 μm) for broader-context information at the microscale, and FIBSEM 3D tomography and SEM and TEM for finer-scale information at the nanometer-to-micrometer scale, as we have done previously for lamellar bone [24,35,36]. Here we provide an integrated, correlative, 3D description of the structural

relationships in Achilles enthesis where both organic and inorganic constituents contribute greatly to macro-level function of the enthesis. For mouse Achilles enthesis, we examined this in both normal fibrocartilaginous tissue (WT) and in osteomalacic fibrocartilaginous tissue (*Hyp*).

Recent progress in our understanding of mineralization mechanisms working at the nanoscale, and mineral structuring/patterning occurring at the microscale, has partly stemmed from our more fully
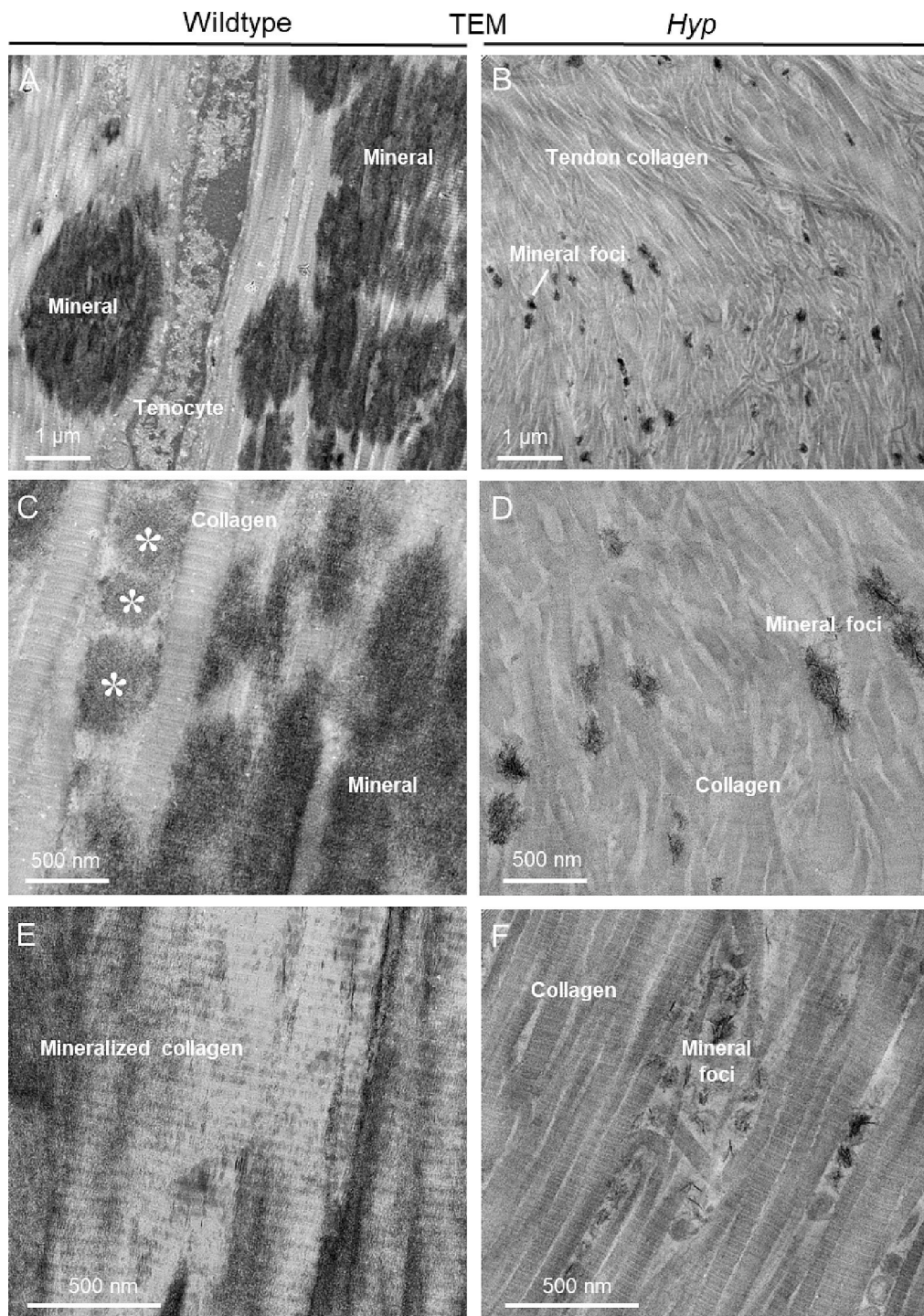
13

Fig. 10. TEM of Achilles calcifying tendinopathy in WT and *Hyp*. (**A, C, E**) Crossfibrillar mineral tessellation in Achilles tendon in WT mice. Mineralization of the Achilles tendon, beginning as smaller mineral foci, enlarge along the collagen trajectory and across collagen fibrils to become abutting crossfibrillar mineral tesselles. Their long axis aligns with the long axis of collagen (A). More spherulitic deposits of mineral (asterisks) are often found between the collagen fibrils (C), and mineral crystals register with the collagen banding pattern (E). (**B, D, F**) Lack of distinct crossfibrillar mineral tessellation in Achilles tendon of *Hyp* mice. Unlike the mineral tessellation that occurs in WT tendon, *Hyp* tendon shows predominantly scattered calcification as numerous widely scattered small foci, again with many nucleation sites seemingly between collagen fibrils. Despite the defect in mineral tessellation in *Hyp* mice, the accumulation of many small foci in different areas still lead to large swaths of mineralized tendon (see previous Figs. 9C, E, G). All images from 12-month-old mice.

understanding the role of enzymes such as TNAP and PHEX in removing mineralization inhibitors such as pyrophosphate (PPi) and osteopontin (OPN), respectively [16,31,62–64]. In addition to the previously mentioned broad release of inhibition of mineralization by degradation of inhibitory PPi that occurs through the enzymatic actions of the phosphatase TNAP, we have hypothesized that another substrate-enzyme pair — OPN and PHEX — acts to refine mineralization at the nano- and microscales. Unlike rapid small-molecule (PPi) degradation resulting from TNAP enzymatic activity, refinement of mineralization patterning is proposed to occur through a more extended process of mineralization-inhibiting phosphoprotein synthesis and secretion (e.g. OPN) and subsequent degradation over time into small inactive peptides

via PHEX enzymatic activity [31,62]. Through this degradative inactivation mechanism, release of mineralization inhibition occurring through either direct crystal binding [65,66] or through release from stabilization of transient precursor phases [67,68] is considered to be a regulatory process for mineralization. This notion is supported by in vivo genetic evidence of aberrant mineralization phenotypes in many transgenic (including compound mutants) and spontaneous-mutation mouse models, by immunohistochemical localization of these proteins, and by in vitro biochemical and mineralization assays of their inhibitory and enzymatic activities [31,62].

Building upon previous work done originally in bone [24,69], here we add a multiscale 3D analysis of two more distinct mineralizing
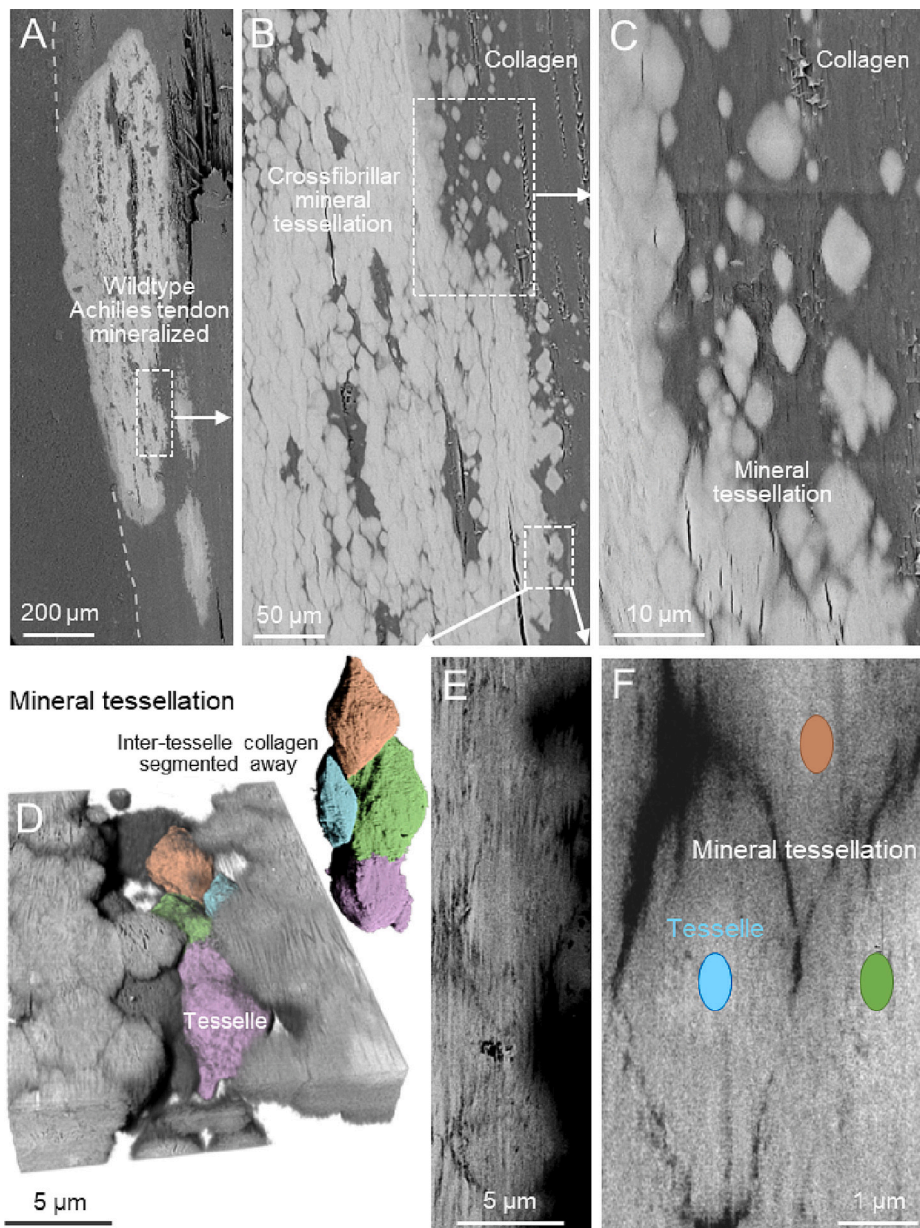
Fig. 11. Wildtype mouse Achilles midsubstance tendon and crossfibrillar mineral tessellation. FIB-SEM region-of-interest selection and serial-surface-view volume correlation from the same block as shown in Fig. 9D. (**A–C**) Block face SEM-BSE images at the periphery of the calcifying tendinopathy in the WT Achilles tendon show somewhat more "faceted" edges of the tesselles than observed in bone and fibrocartilage, but which similarly closely pack into a tessellation pattern, with some tesselles being as large as 5 μm in their long axis. (**D**) FIB-SEM 3D reconstruction from the white boxed region in panel B, and segmentation of a cluster of tesselles from the mineralized tendon interior. (**E, F**) 2D FIB-SEM slices showing interlocking and jagged-edged abutting of tesselles, with persistent boundaries. Colored ovals labeling tesselles in panel F correspond to the colors used in panel D. All images from 12-month-old mice. (For interpretation of the references to color in this figure legend, the reader is referred to the web version of this article.)

collagenous extracellular matrices — calcified enthesis fibrocartilage, and ectopic age-related mineralization of the midsubstance Achilles tendon — and provide evidence in mice of structural alterations in mineral packing that relate to the pathobiology of calcifying enthesopathy observed in *Hyp*/XLH. In normal WT lamellar bone and in calcified fibrocartilage, at or near the mineralization front, fields of small nanometer-sized mineral foci (whose exact origins remain unknown) enlarge into space-filling abutting prolate ellipsoids (geometric approximation) of mineral to form the micrometer-scale pattern of crossfibrillar mineral tessellation. As part of this 3D packing of tesselles, narrow discontinuities persist as discrete boundaries of tens-to-hundreds of nanometers in width, and they remain largely intact throughout the tissues. We have proposed that this type of tessellation patterning over three dimensions — a regular occurrence in different bones of different species [24,31,70–75] — ensures toughness by accommodating excessive deformations. Mineral tessellation has recently been classified as a regular component of bone's hierarchal organization [32]. Here in this study, we have identified this same feature in enthesis calcified fibrocartilage with some structural differences, suggesting that crossfibrillar

mineral tessellation has evolved to be modular, where tesselle spacing and size may simply reflect the density and pseudo-regularity of foci distribution. It is also possible that these parameters of mineral tessellation may vary amongst different vertebrate species as an adaptation to functional demands. Equally important to the mineral tessellation trajectory may be the nature and properties of the tesselle boundaries [51,76]. Specifically concerning crossfibrillar mineral tessellation at the Achilles enthesis, we provide structural evidence which supports its contribution to the stiffness gradient. This likely represents a fine-grained structural mechanism for reducing stress between flexible tendon and stiff bone. This notion is supported by work indicating that failure at the insertion site frequently occurs through bone avulsion, and not within the fibrocartilage zones of the enthesis [55].

In hypomineralized/osteomalacic *Hyp* bone, crossfibrillar mineral tessellation is delayed and incomplete [24]. In the present study comparing WT mineral structural features in Achilles enthesis calcified fibrocartilage to those observed in *Hyp* mice, to our surprise, mineral tessellation in *Hyp* bone, fibrocartilage and midsubstance tendon had nearly identical deficiencies (as compared to WT) in the trajectory of

mineralization within each unique matrix type, apparently reflecting shared regulatory mechanisms in connective tissues. Mineralization of fibrocartilage and midsubstance tendon in *Hyp* mice showed delayed growth at mineral foci, and incomplete space-filling tessellation, just as in *Hyp* bone. Since PHEX activity is absent in *Hyp* mice, and mineralization-inhibiting OPN thus accumulates at sites where it is expressed and secreted as we have shown here by immunohistochemistry in the calcified fibrocartilage zone of the *Hyp* enthesis, this accumulation likely contributes to the mineralization defect in conjunction with the hypophosphatemia. While OPN was readily detectable and abundant by immunohistochemistry in both WT and *Hyp* calcified fibrocartilage, PHEX was not detected in the WT enthesis. This lack of PHEX immunostaining in the WT enthesis fibrocartilage represents either epitope masking of some sort in this particular tissue compared to bone (where there was indeed an expected positive reaction), or that the fibrochondrocytes do not express PHEX. The consistency of strong OPN immunostaining at all mineralization sites examined here (bone, enthesis calcified cartilage, and calcified midsubstance tendon) in both WT and *Hyp* mice provides indirect evidence that matrix OPN levels are regulated (and may become dysregulated) in mineralized tissues to influence mineralization trajectories. This is consistent with abundant literature on OPN acting in this mineralization-inhibiting regulatory capacity for physiologic and ectopic calcification [31,62,77,78]. In fact, as shown for healthy WT bone, in addition to OPN being degraded/inactivated by PHEX enzymatic activity [63,79], there are also other factors that may influence the expression of OPN, such as Pi, PPi, FGF23 and 1,25-dihydroxyvitamin D levels [80–82], to name only a few.

Amongst likely others, two possible explanations (as suggested largely from previous work on bone) for the altered mineralization trajectory occurring at the Achilles enthesis of the *Hyp* mouse are *i*) altered regulation of an as-yet-unknown enthesis mineralization-associated protein, peptide, or molecule (including additional unknown regulatory substrate-enzyme pairings [23,31,62,83], and/or *ii*) inadequate free phosphate available for mineralization. At the Achilles entheses in *Hyp* mice, the expansion of calcifying fibrochondrocytes producing TNAP (expressing *Alpl*) to remove mineralization-inhibiting PPi broadly supports the expansion of mineralization and gradual encroachment of the mineralization front further and further into what would normally be uncalcified fibrocartilage — this potentially proceeding to the formation of overt enthesophytes. However, broad accumulation of inhibitory PPi has also been shown to occur in the tissues of *Hyp* mice [80,84], also near the mineralization front, and this also potentially acts to upregulate OPN [81].

In reconciling the similar aberrant trajectories of mineralization between bone, the enthesis, and that occurring ectopically in the more proximal midsubstance Achilles tendon, it seems reasonable to consider that directly adjacent to fibrochondrocytes, at or slightly beyond the mineralization front within the uncalcified fibrocartilage, compensatory TNAP activity could act to increase the Pi:PPi ratio [16] to the point of permitting mineralization initially in the matrix immediately surrounding the fibrochondrocyte lacunae. This could also potentially occur in tendon where calcification appears ectopically adjacent to tenocytes. Therefore, during ectopic mineralization expanding into the uncalcified fibrocartilage zone of *Hyp* entheses and occurring in midsubstance Achilles tendon, mineralization occurs initially preferentially circumscribing fibrochondrocyte cells, or diffusely nearby tenocytes, respectively. The mineralization then becomes more confluent at a time when constitutive expression of *Alpl*/TNAP by many cells might reach a level sufficient to create a matrix environment that more broadly has a Pi:PPi ratio conducive to mineralization.

4.2. Progression of calcifying enthesopathy in the osteomalacic *Hyp* mouse model of XLH

As a result of inherited inactivating mutations in the *PHEX* gene, XLH patients and *Hyp* mice have soft, hypomineralized bones and teeth

[22–25]. This is attributable to both an increase in systemic circulating FGF23 levels causing hypophosphatemia through renal phosphate wasting coupled with abnormally low-to-normal 1,25-dihydroxyvitamin D levels [29], and an accumulation of mineralization-inhibiting OPN protein locally in the extracellular matrix (as a result of decreased PHEX enzyme activity; OPN is a substrate for PHEX [63]). These changes manifest clinically in bone as vitamin D-resistant rickets, osteomalacia and peri-osteocytic lesions [23], and in teeth as odontomalacia [23,83]. We have previously used FIB-SEM tomography to identify in *Hyp* mouse bone a delayed and defective mineralization trajectory/patterning different from the normal trajectory called crossfibrillar mineral tessellation in lamellar bone. Mineral patterning (tessellation) at the micro- and nanoscale in normal bone has generally been overlooked until recently because it is not resolved by light microscopy or μCT. This space-filling, tessellated pattern of mineral close-packing observed at the microscale in bone has just been revealed from the recent application of FIB-SEM tomographic imaging and 3D reconstruction methods at the high-resolution scale of electron microscopy [24,31,74]. In addition to having aberrant crossfibrillar mineral tessellation, bone deformities and frequent fractures/pseudofractures, XLH patients and *Hyp* mice commonly have expansion of the calcified fibrocartilage zone at the Achilles tendon insertion site (enthesis) leading to calcifying enthesopathy causing additional debilitating pain and loss of mobility for patients [26–28]. Several studies have addressed the underlying molecular mechanisms of calcifying enthesopathy using the *Hyp* mouse model of XLH [14,15,30,33,34].

Beyond the differentiation of progenitor cell populations into differentiated cells in the mineralized tissues of the skeleton and dentition, an important factor in permitting bulk mineralization of extracellular matrices is the broad release from inhibition imposed by the small molecule pyrophosphate (PPi). This release from inhibition (inhibiting an inhibitor) occurs through the enzymatic activity of TNAP (tissue-nonspecific alkaline phosphatase, also abbreviated TNSALP and ALPL; gene *ALPL*) which degrades inhibitory PPi [16] allowing mineralization to proceed according to the *Stenciling Principle* [31,62]. This principle refers to the double-negative paradigm of inhibiting an inhibitor, as originally described by Jacob and Monod (repressing a repressor) for the genetic regulation of enzyme expression in bacteria [85]. For mineralized tissues, several enzyme-substrate pairs following this principle have been identified in mineralized tissues that include the pairs TNAP-PPi and PHEX-OPN [31,62].

In Achilles enthesis fibrocartilage, Liang et al [15] observed an expansion of TNAP-producing cells in female *Hyp* mice as compared to WT mice. This cellular expansion of TNAP production (*Alpl* expression) occurs in conjunction with an expansion of fibrocartilage extracellular matrix markers such as collagen type 2 and an egression/advancement of the mineralization front into the uncalcified fibrocartilage zone [15]. At this site, Karaplis et al [14] reported expansion of TNAP-producing cells at the Achilles insertion of transgenic mice overexpressing *Fgf23*, with PHEX retaining its functionality [14]. Both of the aforementioned studies discuss the fact that tenocytes and fibrochondrocytes express *Fgfr3* and *Klotho*, this having the implication that heightened levels of FGF23 may be involved in the pathogenesis of XLH/*Hyp* enthesopathy. Additional studies by Liu et al [34] in *Hyp* mice identified *Scx-* and *Sox9-* expressing progenitor cells at the Achilles enthesis as was originally described by the Zelzer group for normal mice [7,86]. Of note, Liu et al [34] showed that early treatment (before 2 weeks of age) of *Hyp* mice with 1,25-dihydroxyvitamin D, or with anti-FGF23 antibody, appear to reduce Achilles enthesopathy despite vitamin D increasing circulating FGF23. These findings challenged the prior notion of increased circulating FGF23 as being the primary driver of enthesopathy whether in FGF23 transgenic mice, in *Hyp* mice and XLH patients, or in DMP1-deficient mice where enthesopathy also occurs in a state of elevated circulating FGF23 [87]. Furthermore, Liu et al [34] propose that the lapse in 1,25-dihydroxyvitamin D increases expression of *Bmp* and *Ihh* target genes, this underlying the subsequent expansion of TNAP

expression to additional mature fibrochondrocytes. Indeed, hedgehog signaling is a well-documented essential pathway which governs enthesis development and mineralization [8].

In parallel with these descriptions of aberrant molecular pathways present in *Hyp*/XLH, altered mechanics as a result of defective mineralization in the bone-calcified fibrocartilage complex of entheses has also been implicated in the pathogenesis of calcifying enthesopathy in XLH/*Hyp* [33]. Over the course of Achilles enthesis development in XLH/*Hyp*, it is expected that the forces experienced by Achilles insertion fibrocartilage directly attached to a softer-than-usual, more pliant osteomalacic bone would be far different from that in normally developed entheses (in humans, mice and otherwise). Based on the known role of mechanical stimulation in development of the "enthesis organ" [5,88,89], this alone would be expected to alter developmental, structural and functional aspects of the insertion itself as compared to a normal unaffected enthesis.

Particularly in the context of defective mineralization in *Hyp*/XLH, our results provide new 3D context into calcifying enthesopathy in *Hyp* mice linking the mineralization trajectory in fibrocartilage with micro- and nanoscale 3D structure at the enthesis insertion site. As part of this analysis, using μCT and the higher resolution of sample block face SEM-BSE, we found it difficult to discriminate overt calcifying enthesophytes in *Hyp* mice compared to what has been reported in the literature about the prevalence of this phenotype in human patients (as assessed by conventional radiography). As shown in the 7-, 10.5-, and 14-month mouse ages we examined, as compared to normal WT mice, there is minor protrusion of the calcified fibrocartilage in *Hyp* mice mainly at the plantar fascia insertion into the inferior calcaneal tubercle, with only minor expansion of mineralization occasionally at the superior Achilles insertion. The noticeable expansion of calcified fibrocartilage into the plantar fascia uncalcified fibrocartilage shown in some *Hyp* mice seems to start as a thin rim of mineralization immediately surrounding the lacunae of fibrochondrocytes within the uncalcified fibrocartilage zone, expanding from there to become more confluent to form the more apparent mineral protrusions. We note in the 2D X-ray projections from *Hyp* mice in Faraji-Bellée et al [30] that it was likewise the expansion of calcified fibrocartilage within the plantar fascia that was most evident, this compared to the more prominent calcified spurs in human patients occurring at both the superior and inferior calcaneal tubercles. Also, in this same report, and as we noted in our study, calcifying enthesophytes were not consistently observed [30].

Differences in the prevalence of calcifying enthesophytes between mice and humans could be explained by the different loading conditions of the mode of ambulation between quadrupedal and bipedal species. Ground reaction forces from locomotion influence the loading environment for any long bone, where the orientation and magnitude of the forces partly determine the strain experienced by the bone [90]. It would indeed then seem quite reasonable to consider that in species such as mice — where the metatarsals are lengthened and the calcaneus does not normally contact the surface during walking — the mechanical forces applied to the calcaneal entheses would be different from those found in humans, and likely even more so for conditions such as the osteomalacias having defective mineralization.

In addition to this difference in prevalence and appearance of calcifying enthesophytes between XLH patients and *Hyp* mice, also observed was extensive and consistent age-related calcifying tendinopathy in the midsubstance region of the Achilles tendon proper, in both normal WT and *Hyp* mice, and starting at 7 months of age. While this was a consistent finding in our aged mouse groups, and in a recent study from another group on rat tendon [91], this is a rare occurrence in older human adults [92,93]. Despite low prevalence in humans, calcifying tendinopathy increases risk and worsens clinical outcomes of tendon rupture [93]. Distinct differences in the occurrence of ectopic calcifications between human and mouse, and in other species, support the broader notion of how anatomy and lifestyle differences predispose connective tissues distinctly to ectopic calcifications, and those which

originate from both disease and aging. Taken together, our findings generally reinforce our understanding of the importance of altered mechanics in the pathogenesis of XLH/*Hyp* calcifying enthesopathy. These may act in addition to the aforementioned influences from high circulating FGF23 and/or low-to-normal 1,25-dihydroxyvitamin D on fibrochondrocyte maturation and function, all of which influence mineralization trajectories in the mineralized tissues of entheses.

4.3. Calcifying tendinopathy in the Achilles tendon proper (midsubstance)

In the Achilles midsubstance tendon we documented consistent age-related mineralization (calcifying tendinopathy) in both WT and *Hyp* mice located almost exclusively in the anterior region of the tendon, and sometimes with merging calcifying masses at the scale of hundreds of micrometers. This general location where calcification seems to preferentially initiate was also documented in a recent study in rats of even younger age (3 months), and in females [91]. Moreover, using 2D and 3D electron microscopy methods to examine the nano- and microscale features of this ectopic calcification, we show in WT mice that like in bone and in enthesis fibrocartilage, the mineralization similarly follows a crossfibrillar mineral tessellation pattern. This pattern in tendon midsubstance again arises from a mineralization trajectory that starts with small mineral foci in the collagenous extracellular matrix that then expand into abutting tesselles. In *Hyp* mice, again, similar to bone and fibrocartilage, an ultrastructural mineralization deficiency was observed that likewise leads to altered mineral tessellation, with mineral foci nucleation favored over mineral foci growth, thus leaving abundant small foci and aborted tesselles as compared to the WT midsubstance calcification. Like for the other mineralized tissues examined in this study, OPN was abundant at this calcifying site. Additional studies on this newly found, consistently present, ectopic tendon calcification site in aged mice are required to examine other factors that might be involved. Moreover, this site offers a readily available in vivo mammalian calcification model for examining calcium-phosphate mineralization events in a highly anisotropic collagenous extracellular matrix assembly, in addition to the avian tendon calcification model [73,94].

4.4. Concluding comments

Prior to the availability of methods for 3D ultrastructural research as is the topic of this investigation, John Currey — when writing on the heterogeneity of bone — postulated that "The ideal situation would seem to have bone filled with coherent, reasonably strong interfaces, which will behave elastically, but which open up if a dangerous crack nears them, and which lie in such an orientation that the crack growth is impeded" [95]. Now, with the advent of new sample processing methods, 3D imaging instrumentation and advanced software algorithms for deep learning-based segmentation and analysis tools [47], new coherent and continuous organic-inorganic interfaces and structure have been revealed to persist deep into mineralized tissues, and into old age. As part of crossfibrillar mineral tessellation in these tissues, differing degrees of tesselle size, spacing, and fusion do exist depending on the tissue, and on the location within a given tissue [51,72,76]. Indeed, 2D and 3D space-filling mineral tessellation with repeating units of alternating pliant and stiff elements appears to be a strategy widely present in biology to provide combined strength and toughness [61,96–99]. The recent ability to circumvent the inherent trade-off between high resolution and broad context is resulting in continuous and seamless structural imaging data that is providing new functional mechanistic insight into biological assemblies characterized in three dimensions over multiple magnification scales. Here, we were able to characterize in 3D the similarity of the mineralization pattern in distinct tissues: enthesis, tendon and bone. Likewise, we characterized a strikingly consistent deviation of the mineralization pattern in ectopic mineralization using a mouse model (*Hyp*) of osteomalacia, where the

molecular determinants of the *Stenciling Principle* for extracellular matrix mineralization are missing one of their key players (PHEX).

Supplementary data to this article can be found online at https://doi.org/10.1016/j.bone.2023.116818.

CRediT authorship contribution statement

Daniel J. Buss: Conceptualization, Data curation, Formal analysis, Investigation, Methodology, Validation, Visualization, Writing – original draft, Writing – review & editing. **Katya Rechav:** Investigation, Writing – review & editing. **Natalie Reznikov:** Conceptualization, Formal analysis, Investigation, Methodology, Software, Supervision, Validation, Visualization, Writing – review & editing. **Marc D. McKee:** Conceptualization, Data curation, Formal analysis, Funding acquisition, Investigation, Methodology, Project administration, Resources, Supervision, Validation, Visualization, Writing – review & editing.

Declaration of competing interest

All authors indicate that they have no disclosures to make, or any conflicts of interest pertaining to this work.

Data availability

Data will be made available on request.

Acknowledgements

References

[1] S. Thomopoulos, V. Birman, G. Genin, The challenge of attaching dissimilar materials, in: Structural Interfaces and Attachments in Biology, 1 ed., Springer, New York, 2013, pp. 3–17.

[2] A. Tits, Attaching Soft to Hard: A Multimodal Correlative Investigation of the Tendon-Bone Interface, University of Liege, 2023.

[3] J. Apostolakos, T.J. Durant, C.R. Dwyer, R.P. Russell, J.H. Weinreb, F. Alaee, K. Beitzel, M.B. McCarthy, M.P. Cote, A.D. Mazzocca, The enthesis: a review of the tendon-to-bone insertion, Muscles Ligaments Tendons J. 4 (3) (2014) 333–342.

[4] L. Rossetti, L.A. Kuntz, E. Kunold, J. Schock, K.W. Muller, H. Grabmayr, J. Stolberg-Stolberg, F. Pfeiffer, S.A. Sieber, R. Burgkart, A.R. Bausch, The microstructure and micromechanics of the tendon-bone insertion, Nat. Mater. 16 (6) (2017) 664–670.

[5] H.M. Shaw, M. Benjamin, Structure-function relationships of entheses in relation to mechanical load and exercise, Scand. J. Med. Sci. Sports 17 (4) (2007) 303–315.

[6] A. Thambyah, N.D. Broom, The enthesis, The Soft–Hard Tissue Junction: Structure, Mechanics and Function, Cambridge University Press, Cambridge, 2018, pp. 283–348.

[7] E. Zelzer, E. Blitz, M.L. Killian, S. Thomopoulos, Tendon-to-bone attachment: from development to maturity, Birth Defects Res. C Embryo Today 102 (1) (2014) 101–112.

[8] F. Fang, M. Sup, A. Luzzi, X. Ferrer, S. Thomopoulos, Hedgehog signaling underlying tendon and enthesis development and pathology, Matrix Biol. 105 (2022) 87–103.

[9] H. Murata, H. Nishizono, M. Miyoshi, Postnatal development of structure and arrangement of tendon cells. A scanning and transmission electron microscope study in the rat calcaneal tendon, Okajimas Folia Anat. Jpn. 77 (2–3) (2000) 77–86.

[10] T. Kanazawa, M. Gotoh, K. Ohta, N. Shiba, K. Nakamura, Novel characteristics of normal supraspinatus insertion in rats: an ultrastructural analysis using three-dimensional reconstruction using focused ion beam/scanning electron microscope tomography, Muscles Ligaments Tendons J. 4 (2) (2014) 182–187.

[11] M. Benjamin, J.R. Ralphs, Fibrocartilage in tendons and ligaments—an adaptation to compressive load, J. Anat. 193 (Pt 4) (1998) 481–494.

[12] D.P. Cury, F.J. Dias, M.A. Miglino, I.S. Watanabe, Structural and ultrastructural characteristics of bone-tendon junction of the calcaneal tendon of adult and elderly wistar rats, PLoS One 11 (4) (2016), e0153568.

[13] R. Marinovich, Y. Soenjaya, G.Q. Wallace, A. Zuskov, A. Dunkman, B.L. Foster, M. Ao, K. Bartman, V. Lam, A. Rizkalla, F. Beier, M.J. Somerman, D. W. Holdsworth, L.J. Soslowsky, F. Lagugné-Labarthet, H.A. Goldberg, The role of bone sialoprotein in the tendon-bone insertion, Matrix Biol. 52-54 (2016) 325–338.

[14] A.C. Karaplis, X. Bai, J.P. Falet, C.M. Macica, Mineralizing enthesopathy is a common feature of renal phosphate-wasting disorders attributed to FGF23 and is exacerbated by standard therapy in hyp mice, Endocrinology. 153 (12) (2012) 5906–5917.

[15] G. Liang, L.D. Katz, K.L. Insogna, Carpenter TO, C.M. Macica, Survey of the enthesopathy of X-linked hypophosphatemia and its characterization in Hyp mice, Calcif. Tissue Int. 85 (3) (2009) 235–246.

[16] J.L. Millan, M.P. Whyte, Alkaline phosphatase and hypophosphatasia, Calcif. Tissue Int. 98 (4) (2016) 398–416.

[17] A.C. Deymier, Y. An, J.J. Boyle, A.G. Schwartz, V. Birman, G.M. Genin, S. Thomopolous, A.H. Barber, Micro-mechanical properties of the tendon-to-bone attachment, Acta Biomater. 56 (2017) 25–35.

[18] A.G. Schwartz, J.D. Pasteris, G.M. Genin, T.L. Daulton, S. Thomopoulos, Mineral distributions at the developing tendon enthesis, PLoS One 7 (11) (2012), e48630.

[19] K.L. Moffat, W.H. Sun, P.E. Pena, N.O. Chahine, S.B. Doty, G.A. Ateshian, C. T. Hung, H.H. Lu, Characterization of the structure-function relationship at the ligament-to-bone interface, Proc. Natl. Acad. Sci. U. S. A. 105 (23) (2008) 7947–7952.

[20] Y. Hu, V. Birman, A. Deymier-Black, G. Schwartz, Thomopoulos S. Andrea, M. Genin, Guy., Stochastic Interdigitation as a toughening mechanism at the Interface between tendon and bone, Biophys. J. 108 (2) (2015) 431–437.

[21] L. Zhao, A. Thambyah, N.D. Broom, A multi-scale structural study of the porcine anterior cruciate ligament tibial enthesis, J. Anat. 224 (6) (2014) 624–633.

[22] B.R. Coyac, G. Falgayrac, G. Penel, A. Schmitt, T. Schinke, A. Linglart, M.D. McKee, C. Chaussain, C. Bardet, Impaired mineral quality in dentin in X-linked hypophosphatemia, Connect. Tissue Res. 59 (sup1) (2018) 91–96.

[23] T. Boukpessi, B. Hoac, B.R. Coyac, T. Leger, C. Garcia, P. Wicart, M.P. Whyte, F. H. Glorieux, A. Linglart, C. Chaussain, M.D. McKee, Osteopontin and the dento-osseous pathobiology of X-linked hypophosphatemia, Bone 95 (2017) 151–161.

[24] D.J. Buss, N. Reznikov, M.D. McKee, Crossfibrillar mineral tessellation in normal and Hyp mouse bone as revealed by 3D FIB-SEM microscopy, J. Struct. Biol. 107603 (2020).

[25] N. Fratzl-Zelman, S. Gamsjaeger, S. Blouin, R. Kocijan, P. Plasenzotti, S. Rokidi, K. Nawrot-Wawrzyniak, K. Roetzer, G. Uyanik, G. Haeusler, E. Shane, A. Cohen, K. Klaushofer, E.P. Paschalis, P. Roschger, P. Fratzl, J. Zwerina, E. Zwettler, Alterations of bone material properties in adult patients with X-linked hypophosphatemia (XLH), J. Struct. Biol. 211 (3) (2020), 107556.

[26] J. Herrou, A.S. Picaud, L. Lassalle, L. Pacot, C. Chaussain, V. Merzoug, A. Hervé, M. Gadion, A. Rothenbuhler, P. Kamenický, C. Roux, A. Linglart, M.B. Duplan, K. Briot, Prevalence of enthesopathies in adults with X-linked hypophosphatemia: analysis of risk factors, J. Clin. Endocrinol. Metab. 107 (1) (2022) e224–e235.

[27] A. Steele, R. Gonzalez, J.C. Garbalosa, K. Steigbigel, T. Grgurich, E.J. Parisi, R. S. Feinn, S.M. Tommasini, C.M. Macica, Osteoarthritis, osteophytes, and enthesophytes affect biomechanical function in adults with X-linked hypophosphatemia, J. Clin. Endocrinol. Metab. 105 (4) (2020).

[28] F.H. Glorieux, L.F. Bonewald, N.C. Harvey, M.C.H. van der Meulen, Potential influences on optimizing long-term musculoskeletal health in children and adolescents with X-linked hypophosphatemia (XLH), Orphanet. J. Rare Dis. 17 (1) (2022) 30.

[29] A. Gohil, E.A. Imel, FGF23 and associated disorders of phosphate wasting, Pediatr. Endocrinol. Rev. 17 (1) (2019) 17–34.

[30] C.A. Faraji-Bellee, A. Cauliez, B. Salmon, O. Fogel, V. Zhukouskaya, A. Benoit, T. Schinke, C. Roux, A. Linglart, C. Miceli-Richard, C. Chaussain, K. Briot, C. Bardet, Development of enthesopathies and joint structural damage in a murine model of X-linked hypophosphatemia, Front Cell. Dev. Biol. 8 (2020) 854.

[31] M.D. McKee, D.J. Buss, N. Reznikov, Mineral tessellation in bone and the stenciling principle for extracellular matrix mineralization, J. Struct. Biol. 214 (1) (2022), 107823.

[32] D.J. Buss, R. Kroger, M.D. McKee, N. Reznikov, Hierarchical organization of bone in three dimensions: a twist of twists, J. Struct. Biol. X 6 (2022), 100057.

[33] C.M. Macica, J. Luo, S.M. Tommasini, The enthesopathy of XLH Is a mechanical adaptation to osteomalacia: Biomechanical evidence from Hyp mice, Calcif. Tissue Int. 111 (3) (2022) 313–322. Sept.

[34] E.S. Liu, J.S. Martins, W. Zhang, M.B. Demay, Molecular analysis of enthesopathy in a mouse model of hypophosphatemic rickets, Development 145 (15) (2018).

[35] E.A. Zimmermann, I.A.K. Fiedler, B. Busse, Breaking new ground in mineralized tissue: assessing tissue quality in clinical and laboratory studies, J. Mech. Behav. Biomed. Mater. 113 (2021), 104138.

[36] N.K. Wittig, M. Ostergaard, J. Palle, T.E.K. Christensen, B.L. Langdahl, L. Rejnmark, E. Hauge, A. Bruel, J.S. Thomsen, H. Birkedal, Opportunities for

biomineralization research using multiscale computed X-ray tomography as exemplified by bone imaging, J. Struct. Biol. 214 (1) (2021), 107822.

[37] T.A. Grunewald, M. Liebi, N.K. Wittig, A. Johannes, T. Sikjaer, L. Rejnmark, Gao Zirui, M. Rosenthal, M. Guizar-Sicairos, H. Birkedal, M. Burghammer, Mapping the 3D orientation of nanocrystals and nanostructures in human bone: indications of novel structural features, Sci. Adv. 6 (24) (2020), eaba4171.

[38] E.D. Eren, W.H. Nijhuis, F. van der Weel, A. Dede Eren, S. Ansari, P.H.H. Bomans, H. Friedrich, R.J. Sakkers, H. Weinans, G. de With, Multiscale characterization of pathological bone tissue, Microsc. Res. Tech. 85 (2) (2022) 469–486.

[39] T.M. Strom, F. Francis, B. Lorenz, A. Boddrich, M.J. Econs, H. Lehrach, T. Meitinger, Pex gene deletions in Gy and Hyp mice provide mouse models for X-linked hypophosphatemia, Hum. Mol. Genet. 6 (2) (1997) 165–171.

[40] L. Beck, Y. Soumounou, J. Martel, G. Krishnamurthy, C. Gauthier, C.G. Goodyer, H. S. Tenenhouse, Pex/PEX tissue distribution and evidence for a deletion in the 3′ region of the Pex gene in X-linked hypophosphatemic mice, J. Clin. Invest. 99 (6) (1997) 1200–1209.

[41] S. Ichikawa, A.K. Gray, E. Bikorimana, M.J. Econs, Dosage effect of a Phex mutation in a murine model of X-linked hypophosphatemia, Calcif. Tissue Int. 93 (2) (2013) 155–162.

[42] M.F. Lyon, X-chromosome inactivation, Curr. Biol. 9 (7) (1999) R235–R237.

[43] N. Otsu, A threshold selection method from gray-level histograms, IEEE Trans. Syst. Man Cybern. 9 (1) (1979).

[44] N. Reznikov, H. Liang, M.D. McKee, N. Piché, Technical note: mapping of trabecular bone anisotropy and volume fraction in 3D using μCT images of the human calcaneus, Am. J. Biol. Anthropol. 177 (3) (2022) 566–580.

[45] N. Reznikov, R. Almany-Magal, R. Shahar, S. Weiner, Three-dimensional imaging of collagen fibril organization in rat circumferential lamellar bone using a dual beam electron microscope reveals ordered and disordered sub-lamellar structures, Bone. 52 (2) (2013) 676–683.

[46] W.F. Chissoe, E.L. Vezey, J.J. Skvarla, The use of osmium-thiocarbohydrazide for structural stabilization and enhancement of secondary electron images in scanning electron microscopy of pollen, Grana. 34 (5) (1995) 317–324.

[47] N. Reznikov, D.J. Buss, B. Provencher, M.D. McKee, N. Piche, Deep learning for 3D imaging and image analysis in biomineralization research, J. Struct. Biol. 212 (2020) 107598.

[48] F. Crameri, G.E. Shephard, P.J. Heron, The misuse of colour in science communication, Nat. Commun. 11 (1) (2020).

[49] G. Voronoi, Nouvelles applications des paramètres continus à la théorie des formes quadratiques. Premier mémoire. Sur quelques propriétés des formes quadratiques positives parfaites, J. Reine Angew. Math. 1908 (1908) 97–102.

[50] B. Ecarot, M. Desbarats, 1,25-(OH)2D3 down-regulates expression of Phex, a marker of the mature osteoblast, Endocrinology. 140 (3) (1999) 1192–1199.

[51] T. Tang, W. Landis, E. Raguin, P. Werner, L. Bertinetti, M. Dean, W. Wagermaier, P. Fratz, A 3D network of nanochannels for possible ion and molecule transit in mineralizing bone and cartilage, Adv. NanoBiomed. Res. 2 (2022) 2100162.

[52] B. Hoac, M. Ostergaard, N.K. Wittig, T. Boukpessi, D.J. Buss, C. Chaussain, H. Birkedal, M. Murshed, M.D. McKee, Genetic ablation of osteopontin in osteomalacic Hyp mice partially rescues the deficient mineralization without correcting hypophosphatemia, J. Bone Miner. Res. 35 (10) (2020) 2032–2048. Oct.

[53] C.M. Giachelli, S. Steitz, Osteopontin: a versatile regulator of inflammation and biomineralization, Matrix Biol. 19 (7) (2000) 615–622.

[54] A.C. Deymier-Black, J.D. Pasteris, G.M. Genin, S. Thomopoulos, Allometry of the tendon enthesis: mechanisms of load transfer between tendon and bone, J. Biomech. Eng. 137 (11) (2015), 111005.

[55] M. Golman, A.C. Abraham, I. Kurtaliaj, B.P. Marshall, Y.J. Hu, A.G. Schwartz, X. E. Guo, V. Birman, P.J. Thruner, G.M. Genin, S. Thomopolous, Toughening mechanisms for the attachment of architectured materials: mechanics of the tendon enthesis, Sci. Adv. 7 (48) (2021), eabi5584.

[56] A. Tits, D. Ruffoni, Joining soft tissues to bone: insights from modeling and simulations, Bone Rep. 14 (2021), 100742.

[57] A. Tits, E. Plougonven, S. Blouin, M.A. Hartmann, J.F. Kaux, P. Drion, J. Fernandez, G. Harry van Lenthe, D. Ruffoni, Local anisotropy in mineralized fibrocartilage and subchondral bone beneath the tendon-bone interface, Sci. Rep. 11 (1) (2021) 16534.

[58] J. Sartori, H. Stark, Tracking tendon fibers to their insertion - a 3D analysis of the Achilles tendon enthesis in mice, Acta Biomater. 15 (120) (2021) 146–155. Jan.

[59] K. Livanov, L. Yang, A. Nissenbaum, H.D. Wagner, Interphase tuning for stronger and tougher composites, Sci. Rep. 6 (2016) 26305.

[60] S. Weiner, F. Nudelman, E. Sone, P. Zaslansky, L. Addadi, Mineralized biological materials: a perspective on interfaces and interphases designed over millions of years, Biointerphases 1 (2) (2006) P4–P12.

[61] W. Wagermaier, K. Klaushofer, P. Fratzl, Fragility of bone material controlled by internal interfaces, Calcif. Tissue Int. 97 (3) (2015) 201–212.

[62] N. Reznikov, B. Hoac, D.J. Buss, W.N. Addison, N.M.T. Barros, M.D. McKee, Biological stenciling of mineralization in the skeleton: local enzymatic removal of inhibitors in the extracellular matrix, Bone 138 (2020), 115447.

[63] N.M. Barros, B. Hoac, R.L. Neves, W.N. Addison, D.M. Assis, M. Murshed, A. K. Carmona, M.D. McKee, Proteolytic processing of osteopontin by PHEX and accumulation of osteopontin fragments in Hyp mouse bone, the murine model of X-linked hypophosphatemia, J. Bone Miner. Res. 28 (3) (2013) 688–699.

[64] M. Murshed, D. Harmey, J.L. Millan, M.D. McKee, G. Karsenty, Unique coexpression in osteoblasts of broadly expressed genes accounts for the spatial restriction of ECM mineralization to bone, Genes Dev. 19 (9) (2005) 1093–1104.

[65] M.D. McKee, A. Nanci, Osteopontin at mineralized tissue interfaces in bone, teeth, and osseointegrated implants: ultrastructural distribution and implications for

mineralized tissue formation, turnover, and repair, Microsc. Res. Tech. 33 (2) (1996) 141–164.

[66] W.N. Addison, M.D. McKee, ASARM mineralization hypothesis: a bridge to progress, J. Bone Miner. Res. 25 (5) (2010) 1191–1192.

[67] T. Iline-Vul, R. Nanda, B. Mateos, S. Hazan, I. Matlahov, I. Perelshtein, K. Keinan-Adamsky, G. Althoff-Ospelt, R. Konrat, G. Goobes, Osteopontin regulates biomimetic calcium phosphate crystallization from disordered mineral layers covering apatite crystallites, Sci. Rep. 10 (1) (2020) 15722.

[68] M.J. Olszta, X. Cheng, S.S. Jee, R. Kumar, Y.-Y. Kim, M.J. Kaufman, E.P. Douglas, L. B. Gower, Bone structure and formation: a new perspective, Mater. Sci. Eng. R. Rep. 58 (3) (2007) 77–116.

[69] M. Ayoubi, A.F. Tol, R. Weinkamer, P. Roschger, P.C. Brugger, A. Berzlanovich, L. Bertinetti, A. Roschger, P. Fratzl, 3D interrelationship between osteocyte network and forming mineral during human bone remodeling, Adv. Healthc. Mater. (2021) 2100113.

[70] D.M. Binkley, J. Deering, H. Yuan, A. Gourrier, K. Grandfield, Ellipsoidal mesoscale mineralization pattern in human cortical bone revealed in 3D by plasma focused ion beam serial sectioning, J. Struct. Biol. 212 (2) (2020), 107615.

[71] S. Bertazzo, C.A. Bertran, J.A. Camilli, Morphological characterization of femur and parietal bone mineral of rats at different ages, Key Eng. Mater. (2005) 309–311.

[72] F.A. Shah, K. Ruscsak, A. Palmquist, Transformation of bone mineral morphology: from discrete marquise-shaped motifs to a continuous interwoven mesh, Bone Rep. 13 (2020), 100283.

[73] Z. Zou, T. Tang, E. Macias-Sanchez, S. Sviben, W.J. Landis, L. Bertinetti, P. Fratzl, Three-dimensional structural interrelations between cells, extracellular matrix, and mineral in normally mineralizing avian leg tendon, Proc. Natl. Acad. Sci. U. S. A. 117 (25) (2020) 14102–14109.

[74] C. Micheletti, A. Hurley, A. Gourrier, A. Palmquist, T. Tang, F.A. Shah, K. Grandfield, Bone mineral organization at the mesoscale: a review of mineral ellipsoids in bone and at bone interfaces, Acta Biomater. 142 (2022) 1–13.

[75] K. Grandfield, V. Vuong, H.P. Schwarcz, Ultrastructure of bone: hierarchical features from nanometer to micrometer scale revealed in focused ion beam sections in the TEM, Calcif. Tissue Int. 103 (6) (2018) 606–616.

[76] T. Tang, W. Landis, S. Blouin, L. Bertinetti, M.A. Hartmann, A. Berzlanovich, R. Weinkamer, W. Wagermaier, P. Fratzl, Sub-canalicular nanochannel volume is inversely correlated with calcium content in human cortical bone, J. Bone Miner. Res. 38 (2) (2023) 313–325. Feb.

[77] C.M. Giachelli, Inducers and inhibitors of biomineralization: lessons from pathological calcification, Orthod. Craniofacial Res. 8 (4) (2005) 229–231.

[78] J. Sodek, B. Ganss, M.D. McKee, Osteopontin, Crit. Rev. Oral Biol. Med. 11 (3) (2000) 279–303.

[79] W.N. Addison, Y. Nakano, T. Loisel, P. Crine, M.D. McKee, MEPE-ASARM peptides control extracellular matrix mineralization by binding to hydroxyapatite: An inhibition regulated by PHEX cleavage of ASARM, J. Bone Miner. Res. 23 (10) (2008) 1638–1649.

[80] S.K. Murali, O. Andrukhova, E.L. Clinkenbeard, K.E. White, R.G. Erben, Excessive osteocytic Fgf23 secretion contributes to pyrophosphate accumulation and mineralization defect in Hyp mice, PLoS Biol. 14 (4) (2016), e1002427.

[81] W.N. Addison, F. Azari, E.S. Sorensen, M.T. Kaartinen, M.D. McKee, Pyrophosphate inhibits mineralization of osteoblast cultures by binding to mineral, up-regulating osteopontin, and inhibiting alkaline phosphatase activity, J. Biol. Chem. 282 (21) (2007) 15872–15883.

[82] G.R. Beck Jr., B. Zerler, E. Moran, Phosphate is a specific signal for induction of osteopontin gene expression, Proc. Natl. Acad. Sci. U. S. A. 97 (15) (2000) 8352–8357.

[83] M.D. McKee, B. Hoac, W.N. Addison, N.M. Barros, J.L. Millan, C. Chaussain, Extracellular matrix mineralization in periodontal tissues: noncollagenous matrix proteins, enzymes, and relationship to hypophosphatasia and X-linked hypophosphatemia, Periodontol. 63 (1) (2013) 102–122.

[84] A. Buck, V.M. Prade, T. Kunzke, R.G. Erben, A. Walch, Spatial metabolomics reveals upregulation of several pyrophosphate-producing pathways in cortical bone of Hyp mice, JCI Insight 7 (20) (2022).

[85] F. Jacob, J. Monod, Genetic regulatory mechanisms in the synthesis of proteins, J. Mol. Biol. 3 (1961) 318–356.

[86] E. Blitz, A. Sharir, H. Akiyama, E. Zelzer, Tendon-bone attachment unit is formed modularly by a distinct pool of Scx- and Sox9-positive progenitors, Development. 140 (13) (2013) 2680–2690.

[87] O. Makitie, R.C. Pereira, I. Kaitila, S. Turan, M. Bastepe, T. Laine, H. Kroger, W. G. Cole, H. Juppner, Long-term clinical outcome and carrier phenotype in autosomal recessive hypophosphatemia caused by a novel DMP1 mutation, J. Bone Miner. Res. 25 (10) (2010) 2165–2174.

[88] A. Rufai, M. Benjamin, J.R. Ralphs, Development and ageing of phenotypically distinct fibrocartilages associated with the rat Achilles tendon, Anat. Embryol. 186 (6) (1992).

[89] H.M. Shaw, O.T. Vazquez, D. McGonagle, G. Bydder, R.M. Santer, M. Benjamin, Development of the human Achilles tendon enthesis organ, J. Anat. 213 (6) (2008) 718–724.

[90] D. Schmitt, C. Zumwalt, M.W. Hamrick, The relationship between bone mechanical properties and ground reaction forces in normal and hypermuscular mice, J. Exp. Zool. A 313a(6):339-51 (2010).

[91] M. Pierantoni, M. Hammerman, I. Silva Barreto, L. Andersson, V. Novak, H. Isaksson, P. Eliasson, Heterotopic mineral deposits in intact rat Achilles tendons are characterized by a unique fiber-like structure, J. Struct. Biol. X 7 (2023), 100087.

[92] D. Sullivan, A. Pabich, R. Enslow, A. Roe, D. Borchert, K. Barr, B. Cook, A. Brooks, Extensive ossification of the Achilles tendon with and without acute fracture: a scoping review, J. Clin. Med. 10 (16) (2021).

[93] F. Oliva, A.G. Via, N. Maffulli, Physiopathology of intratendinous calcific deposition, BMC Med. 10 (2012) 95.

[94] W.J. Landis, F.H. Silver, The structure and function of normally mineralizing avian tendons, Comp. Biochem. Physiol. A Mol. Integr. Physiol. 133 (4) (2002) 1135–1157.

[95] J. Currey, Structural heterogeneity in bone: good or bad? J. Musculoskelet. Neuronal Interact. 5 (4) (2005) 317.

[96] C. Gao, B.P.J. Hasseldine, L. Li, J.C. Weaver, Y. Li, Amplifying strength, toughness, and auxeticity via wavy sutural tessellation in plant seedcoats, Adv. Mater. 30 (2018), e1800579.

[97] P. Fratzl, O. Kolednik, F.D. Fischer, M.N. Dean, The mechanics of tessellations - bioinspired strategies for fracture resistance, Chem. Soc. Rev. 45 (2) (2016) 252–267.

[98] M.N. Dean, C.G. Mull, S.N. Gorb, A.P. Summers, Ontogeny of the tessellated skeleton: insight from the skeletal growth of the round stingray Urobatis halleri, J. Anat. 215 (3) (2009) 227–239.

[99] B. Achrai, H.D. Wagner, The turtle carapace as an optimized multi-scale biological composite armor - a review, J. Mech. Behav. Biomed. Mater. 73 (2017) 50–67.